



Molecular dynamics study on magnesium hydride nanoclusters with machine-learning interatomic potential

Ning Wang  and Shiping Huang *

State Key Laboratory of Organic-Inorganic Composites, Beijing University of Chemical Technology, Beijing, 100029, China



(Received 23 February 2020; revised 10 May 2020; accepted 15 September 2020; published 30 September 2020)

We introduce a machine-learning (ML) interatomic potential for Mg-H system based on Behler-Parrinello approach. In order to fit the complex bonding conditions in the cluster structure, we combine multiple sampling strategies to obtain training samples that contain a variety of local atomic environments. First-principles calculations based on density functional theory (DFT) are employed to get reference energies and forces for training the ML potential. For the calculation of bulk properties, phonon dispersion, gas-phase H₂ interactions, and the potential energy surface (PES) for H₂ dissociative adsorption on Mg(0001) surfaces, our ML potential has reached DFT accuracy at the level of GGA-PBE, and can be extended by combining the DFT-D3 method to describe van der Waals interaction. Moreover, through molecular dynamics (MD) simulations based on the ML potential, we find that for Mg_nH_m clusters, Mg/MgH_x phase separation occurs when $m < 2n$, and for a cluster with a diameter of about 4 nm, the Mg part of the cluster forms a hexagonal close-packed (hcp) nanocrystalline structure at low temperature. Also, the calculated diffusion coefficients reproduce the experimental values and confirm an Arrhenius type temperature dependence in the range of 400 to 700 K.

DOI: [10.1103/PhysRevB.102.094111](https://doi.org/10.1103/PhysRevB.102.094111)

I. INTRODUCTION

With the rapid development of industry and changes in our lifestyle, global energy consumption has increased dramatically, leading to the depletion of fossil energies. In recent years, finding alternative energy sources has become increasingly urgent. Because of its abundant reserves, high energy density, and zero emission behavior, hydrogen has been regarded as an ideal fuel to solve both energy crisis and greenhouse effect [1,2]. However, gaseous storage of hydrogen requires extremely high-strength pressure vessels, but still has a relatively low volumetric hydrogen storage density of 30 g_H/L. The density of liquid hydrogen can reach 70 g_H/L, but the hydrogen liquefaction process costs too much energy [1,3]. Hydrogen storage using porous materials such as porous carbons and zeolites has excellent reversibility, but their volumetric hydrogen storage capacities are still low since they require large surface areas [4]. Ahmed *et al.* studied nearly half a million metal-organic frameworks (MOFs) and found a volumetric ceiling at about 40 g_H/L [5], barely meeting the standards for on-board applications.

Metal hydrides have been studied extensively for mobile applications due to their safety and high volumetric hydrogen storage capacities [6]. Considering that heavy metals reduce the gravimetric hydrogen storage density, the lightweight MgH₂ possesses both excellent volumetric and gravimetric hydrogen storage capacities of 110 g_H/L and 7.6 wt% [7], and thus attracts more attention. However, a high desorption temperature of about 300 °C is required due to the high thermodynamic stability of MgH₂, and its hydrogen up-

take and release kinetics are not favorable, which restricts its application [8,9]. Efforts have been made to improve the adsorption/desorption characteristics of MgH₂, including catalyst doping, alloying, and nanostructuring [10–13]. In the meantime, an in-depth understanding of the hydrogen adsorption/desorption mechanism is urgently required to guide the modification of the Mg-based hydrogen storage materials.

Using fast-growing computational simulation techniques, we can theoretically study the adsorption and desorption process. First-principles calculations, especially density functional theory (DFT) methods, are widely used these years. However, when the simulation system contains hundreds or thousands of atoms, or when dealing with properties involving excessive timescales, the first-principles methods will no longer be adequate due to their high computational cost. Molecular dynamics (MD) is one of the efficient ways to study the mechanisms of certain microscopic processes. For magnesium hydrides, when MD is performed to simulate large systems or long timescales, the required computational efficiency is difficult to achieve using first-principles methods. Therefore many interatomic potentials have been developed for the Mg-H system, including an embedded atom method (EAM) potential developed by Tanguy and Magnin [14], a reactive force field (ReaxFF) from Cheung *et al.* [15], an angular-dependent potential (ADP) developed by Smirnova *et al.* [16], and a bond order potential (BOP) proposed by Zhou and co-workers [17]. Among these potentials, EAM employs the simplest formalism and is therefore easy to fit, but research has confirmed that it is not suitable for the Mg-H system, since it is mainly designed for close-packed metals [17]. The formalism of BOP is extremely complicated, a well-parameterized BOP is very accurate for structures similar to

*huangsp@mail.buct.edu.cn

the target samples, but it requires quite a lot of effort to expand its applicability.

Machine-learning methods provide novel solutions for building interatomic potentials. Unlike classical potentials that use fixed analytical functions based on physical insights, machine-learning (ML) potentials originate from mathematical models, using forms such as artificial neural network (ANN) [18–21] and Gaussian approximation potential (GAP) framework [22–24], it can achieve both high accuracy and high flexibility, without being limited by the forms of analytical functions. The parametrization of machine-learning model is relatively easier than fitting classical potential functions, and the applicability of the machine-learning potential can simply be increased by adding new samples into the training database, without considering manually adjusting the constraints on parameters. In recent years, numerous machine-learning potentials have been developed, covering metals [25–28], alloys [29–31], metal oxides [32,33], organic compounds [34–36], and so forth, and can be applied to various types of structures such as bulks [37,38], surfaces [25,38,39], and clusters [26,27,30,38].

In this work, we developed a machine-learning interatomic potential for Mg-H system, mainly focusing on the behavior of Mg_nH_m clusters. The rest of this paper is organized as follows. In Sec. II, we describe the construction of our machine-learning potential, including model architecture, reference sampling strategy, training method and computational details. Section III gives the validation on the accuracy and capability of our potential from different aspects. Molecular dynamics simulations are performed in Sec. IV, the structural properties and diffusion behavior of magnesium hydride clusters are discussed. Finally, in Sec. V, we summarize the main conclusions of this paper and share some perspectives on future work.

II. MODEL CONSTRUCTION

A. Machine-learning potential

Artificial neural network is one of the widely used machine-learning models describing molecular systems. To obtain the input vector of ANN, the atomic coordinates are first converted into a set of variables, called descriptors or symmetry functions [19,21,40]. These symmetry functions contain information about the local chemical environment of each atom, and must be numerically invariant with respect to a translation or rotation of the system, or an exchange of the atomic positions of any two atoms of the same element. Next, taking the aforementioned symmetry functions as inputs, atomic energy contribution E_i is calculated from a well-trained neural network. Finally, for an N -atom system, the total energy of the system can be obtained through summing E_i over the number of atoms as below

$$E = \sum_{i=1}^N E_i. \quad (1)$$

In this work, we use a modified version of Behler-Parrinello symmetry functions [19,41], for each atom the radial and angular environments are taken into account.

To ensure that atomic forces can be calculated using analytic derivatives, the symmetry functions need to be continuous and differentiable. To make their values and slopes smoothly vanish at a proper cutoff radius R_c , a cutoff function f_c is introduced [19,42], which commonly formulated as

$$f_c(R_{ij}) = \begin{cases} \frac{1}{2} \left[\cos \left(\frac{\pi R_{ij}}{R_c} \right) + 1 \right] & \text{for } R_{ij} \leq R_c, \\ 0 & \text{for } R_{ij} > R_c, \end{cases} \quad (2)$$

where R_{ij} is the distance between a central atom i and one of its neighbor j .

For the two-body term, the radial symmetry function used here follows the identical form as proposed by Behler and Parrinello [21,25,41,42],

$$G_{i,m}^{\text{Rad}} = \sum_{j \neq i}^{\text{all}} e^{-\eta_r(R_{ij}-R_s)^2} f_c(R_{ij}), \quad (3)$$

which is a sum of Gaussians multiplied by cutoff functions. The values of η_r and R_s affect the width and peak position of the Gaussian functions, respectively. A fixed value of η_r is used in this work, and a set of R_s parameters makes up the radial part of symmetry functions.

As for the angular symmetry function describing the three-body relation, we use a modified version of Behler-Parrinello symmetry function, inspired by the work of Smith *et al.* in Ref. [41]. Compared with Behler's original function, a parameter R_s is added to the exponential term. It helps to make the radial part of the angular symmetry function more sensitive to different atomic distances, and metal hydride systems benefit from it because the distances between H-H, Mg-H and Mg-Mg vary greatly. Centered on atom i , the angular symmetry function take the form

$$G_{i,m}^{\text{Ang}} = 2^{1-\zeta} \sum_{j,k \neq i}^{\text{all}} (1 + \lambda \cos \theta_{ijk})^\zeta \times e^{-\eta_a[(1/2)(R_{ij}+R_{ik})-R_s]^2} f_c(R_{ij})f_c(R_{ik}), \quad (4)$$

where j and k are two neighboring atoms of atom i , θ_{ijk} is the angle formed by atom i , j and k . Two values $+1$ and -1 can be assigned to parameter λ , which changes the peak position of the cosine function. The width of the angular and radial part of the function are controlled by parameters ζ and η_a , respectively.

In the present study, same cutoff radius $R_c = 4.5 \text{ \AA}$ is set for both radial and angular symmetry functions, which is around two times of the first nearest neighbor distance between Mg and H atoms in MgH_2 crystal. Increasing R_c from 4.5 to 6.0 \AA results in little change of the training error, therefore we choose the smaller cutoff radius to reduce the computational complexity. In total, 64 symmetry functions are employed for each element. Eight radial functions are used for both neighboring Mg or H atom, with η_r fixed to 1.0 \AA^{-2} , and 8 different values of R_s that equally spaced from 0 to $7R_c/8$, so as to give 16 radial symmetry functions. As for angular functions, centering at atom i , two neighboring atoms (j, k) can be (Mg, Mg), (Mg, H), or (H, H), with $\eta_a = 0.1 \text{ \AA}^{-2}$, $\zeta = 1.0$, $\lambda = \pm 1$, and R_s use the same 8 values equally spaced from 0 to $7R_c/8$, yielding 48 angular symmetry functions.

The ANN used in this research is based on a typical multilayer feed-forward neural network architecture [19,25]. We use the hyperbolic tangent function as the activation function in the hidden layer. For the output layer, only one neuron is placed to perform a linear combination of the values from the last hidden layer, and then a linear activation function $y = x$ is used instead of a nonlinear one, thus ensuring that the output atomic energy is not limited by the range of function values.

Obviously, when atoms of different elements are placed in the center of the same chemical environment, the atomic energies are different, which means a separate ANN for each element is required [21,42,43]. For the magnesium hydride system, two independent ANNs are trained for Mg and H separately, both of which contain same hyperparameters with manipulated weights.

In MD simulations, forces acting on atoms are required for updating the velocities and atomic positions, they can be calculated through the negative analytic gradients of the total energy. Using the chain rule, the force component $F_{i,\alpha}$ acting on atom i in direction $\alpha = \{x, y, z\}$ with respect to atomic coordinate $R_{i,\alpha}$ is given by [20,21,42,43]

$$\begin{aligned} F_{i,\alpha} &= -\frac{\partial E}{\partial R_{i,\alpha}} \\ &= -\sum_{i=1}^N \frac{\partial E_i}{\partial R_{i,\alpha}} \\ &= -\sum_{i=1}^N \sum_{j=1}^{M_i} \frac{\partial E_i}{\partial G_{i,j}} \frac{\partial G_{i,j}}{\partial R_{i,\alpha}}, \end{aligned} \quad (5)$$

where E is the total energy, E_i is the atomic energy of atom i , N is the number of atoms, M_i is the number of symmetry functions for atom i , and $G_{i,j}$ is the j th symmetry function for atom i .

B. DFT reference samples

Our machine-learning potential is trained from DFT results. It has been theoretically proven that a multilayer feed-forward ANN can approximate any function with arbitrary precision [44], the chemical space that an ANN could handle, however, is governed by the reference samples at input. Different from empirical potential functions, the ANN architecture is not generalized from specific physical models, as a form of interatomic potential, it could only recognize the atomic chemical environment within its training sample spaces, therefore it intrinsically demands a diversified set of reference data covering all regions relevant to its designated applications.

Plenty of methods have been proposed for sampling reference structures, including *ab initio* MD simulations [45–47], metadynamics procedures [48], normal mode sampling (NMS) [41], or adopting global optimization method such as evolutionary algorithm [31,49], stochastic surface walking (SSW) [50–52], and minima hopping method [53]. In this research, we combine the global minimum searching algorithm coalescence kick (CK) [54–57], *ab initio* MD simulations, and an adaptive sampling scheme [20,58] to generate the reference samples. Table I lists the composition of structures contained in the reference database.

TABLE I. Composition of the reference database. N_s is the number of structures for each type, N_{Mg} and N_{H} represent total number of Mg and H atoms of a given structure type, respectively.

Structure type	N_s	N_{Mg}	N_{H}
Clusters:			
Mg_n	1581	29 582	0
H_n	979	0	6302
Mg_nH_m	9888	273 460	297 388
Scaled clusters:			
Mg_n	725	8861	0
Mg_nH_m	1292	15 956	32 182
Crystals:			
hcp-Mg	750	48 000	0
α -MgH ₂	1250	30 000	60 000
β -MgH ₂	1250	40 000	80 000
γ -MgH ₂	750	24 000	48 000
Stressed crystals:			
hcp-Mg	500	60 800	0
α -MgH ₂	1000	24 000	48 000
β -MgH ₂	1000	32 000	64 000
γ -MgH ₂	1000	32 000	64 000
H ₂ gas	1000	0	102000
Total	22 965	618 659	801 872

It should be pointed out that similar structures appeared in the sampling process, which provided redundant structural information, and it was necessary to introduce screening procedures to improve training efficiency. In the literature, geometric comparisons can be measured by defining distance descriptors between structures, such as methods based on the smooth overlap of atomic positions (SOAP) [23,59–62], and methods based on the fingerprint functions [63]. In this work, the similarity check was based on a sorted list D_i of all interatomic distances for sample i . Two samples i and j with the same elemental compositions will be considered similar if

$$\frac{\sum_k |D_i(k) - D_j(k)|}{\frac{1}{2} \sum_k (D_i(k) + D_j(k))} < \delta_{\text{rel}} \quad (6)$$

and

$$\max_k (|D_i(k) - D_j(k)|) < d_{\text{max}}, \quad (7)$$

where k represents each interatomic distance in the list D_i . Two criteria δ_{rel} and d_{max} stand for the relative accumulated difference and maximum difference for distances between two samples, respectively. For samples containing both H and Mg atoms, the above two criteria were calculated for each element separately, and the weighted sums were calculated as the final criteria based on the total number of distances counted in each element. We used relatively tight thresholds $\delta_{\text{rel}} = 0.01$ and $d_{\text{max}} = 0.1 \text{ \AA}$ here, because force is more sensitive to structural changes, and a better description of force can be beneficial to the ANN potential to perform MD simulation.

Since our interest in this study is mainly in magnesium hydride nanoclusters, at the initial stage a set of small Mg_nH_m ($n \leq 28$, $m = 0$ or $2n$) nanoclusters were generated to train a preliminary ANN. CK method [54–57] was employed in this process to create initial cluster structures scattered on the

potential energy surface (PES). This method initially places all atoms randomly in a sufficiently large box, then analyzes the connectivity of atom pairs based on the sum of the covalent radii between the atoms. Next, push all atoms towards the center of mass until there are no fragments in the system. Finally, perform DFT local optimization on the generated structure. A major advantage of the CK method is that it can avoid the generation of fragmented structures as much as possible, which is what we expect during the sampling process. Because the fragmented structure provides information about the atomic chemical environment similar to the smaller clusters that make up the system, it cannot satisfy our original intention of adding larger cluster samples. Although CK method is effective in sampling small clusters with $n \leq 20$, as the size of the magnesium hydride cluster increases, free H_2 molecules inevitably appear, preventing the determination of the structures of fully hydrogenated clusters. It should be noted that the structures containing free H_2 molecules are also useful for the training of ANN. On one hand, they carry the structural information of the partially hydrogenated clusters, on the other hand, they also provide free H_2 molecule samples, and have information about the interaction between Mg_nH_m clusters and H_2 molecules. However, the lack of samples of fully hydrogenated clusters is unacceptable. Therefore, since the previous report has shown that the CK method is less efficient for clusters with a mixed pattern of delocalized and strongly covalent bonding [55], as in the Mg-H system, we added *ab initio* MD simulations to enhance the data sampling.

Clusters of Mg_nH_{2n} were extracted from α -, β -, and γ - MgH_2 crystal lattice by cutting out spheres centered at random coordinates. In the next step, a random selection procedure was performed, removing hydrogen atoms out of the clusters to generate Mg_nH_m ($n \leq 28$, $m = 0, n/2, n, 3n/2, 2n$) clusters. *Ab initio* MD simulations were performed on all these clusters, starting from a heating process of a smooth temperature ramping from 300 to 1000 K, followed by a structure relaxation at 1000 K for 1 ps, the system was then cooled back to 300 K, ended up with another 1 ps MD relaxation at 300 K. Samples were collected from different stages of the MD trajectories, and the heating and cooling processes enabled a more continuous sampling toward different chemical environments.

In order to improve the universality of our potential, MgH_2 crystal structures were included in the reference dataset, which is also beneficial for describing the bulk-like internal structure of large clusters. Tetragonal TiO_2 -rutile-type α - MgH_2 , cubic β - MgH_2 , orthorhombic γ - MgH_2 , and hexagonal close-packed (hcp) hcp-Mg were taken into consideration. Supercells were created to ensure each side of the simulation box larger than 9.0 \AA ($2R_c$), and then *ab initio* MD simulations under NVT ensemble were performed on each crystal structure, with temperatures ranging from 100 to 1800 K. Structures at low temperatures as well as highly distorted structures at high temperatures were both accepted to increase the diversity of sampling environments. Also, samples with purely hydrogen gases were considered as well.

Nevertheless, the ANN trained with the aforementioned samples was not good enough, unreasonably small atomic distances were detected during the MD simulation driven by such potential, and more than two hydrogen atoms tended to

aggregate with each other, which should not happen. This is commonly seen during the training processes of the previously reported machine-learning potentials [64], mainly due to the lack of descriptions of these extreme bonding conditions, although these unreasonable structures are not supposed to be visited in MD simulations, they should be fed to the ANN, and force the ANN learning to avoid leading the simulation systems toward these situations.

Two additional sampling procedures were introduced to improve the overall performance of our machine-learning potential. First, clusters with scaled coordinates and crystals under compressive or tensile strain were calculated using DFT and added to the reference samples. Scaling operation was applied on the selected ones among CK and MD generated clusters. Multiplying all the atomic coordinates in the cluster by a scaling factor, we shorten the atomic distances in the structures. The scaling factor was chosen randomly for each cluster in the range from 0.75 to 1.0, avoiding very small values which produce structures with unnecessary high energies. Single point DFT calculations were then carried out to get the reference energies and atomic forces. *Ab initio* MD simulations on different types of MgH_2 and Mg crystals with reduced or expanded lattices were performed. We applied -5% , -2% , 2% , and 5% triaxial compressive or tensile strain to the supercells of the crystals, similar MD simulations were carried out with fixed cell parameters. These measures provided additional atomic environments to the ANN.

Second, a self-consistent sampling method was introduced to expand the reference data. Manually designed samples are always limited and barely span all relevant regions, it is therefore better to make ANN explore uncovered areas and improve themselves. A direct way is to use the trained preliminary ANN to perform MD simulations on magnesium hydride clusters, and then recalculate the trajectories by using DFT to obtain the reference energies and forces, choose those structures with large deviations and add them into the reference database. This method works well but is time consuming, for those structures that ANN can accurately calculate, additional DFT calculations are not necessary. In this research, a more effective procedure called adaptive sampling scheme [20,58] was employed. This procedure uses an active learning technique based on the query by committee (QBC) approach [65,66]. The idea of the QBC algorithm is to train different models on the same dataset, and use the disagreement in prediction of new candidates by different models to measure the performance. It is helpful to explore the missing structural information and minimize the DFT computational cost. The adaptive sampling method here used a simplified QBC algorithm, only two different models were trained, and the determination of candidate inclusion criteria was based only on experience rather than statistical deviation. Based on the reference samples collected so far, a secondary machine-learning potential was trained with different ANN architecture compared to the previous one. For the local atomic environments included in the reference samples, both ANNs should be able to reproduce accurate energies and forces with minimal variations in between. However, for those regions that ANNs have not learned from, the results calculated from two trained potentials will be different. Initial structures of Mg_nH_m ($n \leq 50$, $m = 0, n/2, n, 3n/2, 2n$) clusters were generated the

same way as previously mentioned except that larger clusters are included. For each adaptive sampling cycle, part of those clusters were selected to perform MD simulations using our initial ANN potential. Temperature was kept constant at 300 K during the MD run, 20 ps simulation with a time step of 1.0 fs produced a trajectory with 20 000 configurations for each cluster. All these configurations were recomputed by the secondary ANN, structures with energy differences larger than a certain threshold were selected for DFT calculations, and were then added to the reference dataset. The threshold was initially set to 50 meV/atom, and gradually reduced to 25 meV/atom. After updating the reference samples, both ANNs were refined by training with the augmented dataset, a new group of clusters were selected from the generated initial structures, entering the next sampling cycle.

Finally, almost a million reference samples were generated, we used the following rules to pick a part from each kind of samples. For structures generated by *ab initio* MD simulations, a snapshot was selected from every 100 steps of each trajectory for clusters, and every 20 steps for crystals. All the local minima obtained by CK optimization that passed the similarity check were selected. As for the clusters with scaled coordinates and the structures generated by the adaptive sampling processes, all the samples that passed the similarity check were added to the final dataset. In the end, a total of 22965 samples were selected, 90% of them made up the training set to train the ANN, the other 10% were treated as test set, or validation set, which kept independent during the training process and used to evaluate the capability of the potential dealing with unknown structures. It is worth noting that in this work, the adaptive sampling procedure mainly served as a method to supplement the missing chemical information, so we used a relatively simple selection strategy. Meanwhile, in the literature, more systematic selection methods adopt algorithms such as CUR matrix decompositions to select relevant and diverse structures [67,68], which can help to perform automatic sampling and active learning processes from the beginning.

C. Potential training

After testing different combinations of the number of hidden layers and the number of neurons, a 64-40-40-1 neural network architecture was chosen, which contains two hidden layers with 40 neurons in each. The ANN was trained to fit both target energies and forces [69,70] by minimizing the following loss function:

$$L = \frac{1}{M} \sum_{i=1}^M \left[\left(\frac{\Delta E_i}{N_i} \right)^2 + \frac{\gamma}{3N_i} \sum_{j=1}^{N_i} \sum_{\alpha=1}^3 \Delta F_{i,j,\alpha}^2 \right], \quad (8)$$

where M is the number of samples, N_i is the number of atoms in sample i , $\Delta E_i = E_i^{\text{DFT}} - E_i^{\text{ANN}}$ is the energy difference between the DFT and ANN results, $\Delta F_{i,j,\alpha} = F_{i,j,\alpha}^{\text{DFT}} - F_{i,j,\alpha}^{\text{ANN}}$ is the error in force acting on atom j in direction $\alpha = \{x, y, z\}$ calculated by DFT and ANN, here $F_{i,j,\alpha}^{\text{ANN}}$ is obtained by taking the gradient of E_i^{ANN} with respect to the atomic coordinates, as described in Eq. (5). This loss function combines the mean square errors (MSE) of both energies and forces, using parameter γ to control the contribution of forces to the total

loss with respect to energies. In this study, $\gamma = 0.3$ was employed. The inclusion of forces in the loss function significantly improved the performance of the machine-learning potential in MD simulations. Limited-memory Broyden-Fletcher-Goldfarb-Shanno (L-BFGS) method was employed to optimize the weights of the ANN. L2 regularization was used to prevent overfitting.

Comparisons between the DFT and our ANN results on energy and force calculations are plotted in Fig. 1. The root mean square errors (RMSEs) of the energies are 30.91 and 31.25 meV/atom for the training and test sets, respectively. As for forces, the RMSE values are 195.9 and 189.9 meV/Å for training and test sets. The very closed values of training and test errors represent a good flexibility of the potential and no overfitting during the training process. Besides, for training and test set, the mean absolute errors (MAEs) of energies are 18.15 and 18.23 meV/atom, while MAEs of forces are 96.10 and 95.48 meV/Å, respectively. It is known that the values of MAE are usually smaller than RMSEs, but the relatively large differences between those values shows that a few samples with large deviations have a significant impact on the evaluation of errors. Considering that we added structures under extreme conditions, such as clusters with scaled coordinates and crystals under compressive or tensile strain, the energies and forces of these samples are beyond the usual range in normal simulation conditions, so we calculated the errors of the training and test set again using the same potential, including those structures generated by CK method and *ab initio* MD simulations only. As a result, the RMSEs of energies of the new training and test set reduced to 18.64 and 18.43 meV/atom, and the RMSEs of forces decreased to 106.6 and 105.6 meV/Å. Note that the outliers in Figs. 1(a) and 1(b) correspond to the added unphysical structures, mainly the structures of H atoms aggregated in the gas phase. These samples play a role in avoiding the appearance of unphysical structures in the simulation, and since they will not be visited under normal simulation conditions, these outliers will not impair the performance of our ANN potential.

Admittedly, the energy errors we obtained is greater than typical values of the reported ML based potentials for other nanosystems [26,27,30,43,71–76], mainly due to the high complexity of the magnesium hydride system and our pursuit of versatility of the potential. The atomic radius of H atom is much smaller than that of Mg atom, which allows H atoms to exist in magnesium hydrides in various forms. Researches on the dehydrogenation process show that the crystalline magnesium hydrides undergo a phase transformation into solid solutions [77,78], in which H atoms can exist at the interstitial sites of Mg atoms and diffuse therein. From this perspective alone, the model of magnesium hydride is much more complicated than those previously reported mainly for metal clusters and nanoalloy systems, which makes it difficult to construct accurate potentials.

Another factor that affects accuracy is the diversity of training samples. The typical energy errors of the ML based potentials reported for nanosystems are around 5–10 meV/atom. For example, Chiriki *et al.* constructed an ANN potential by fitting DFT data for Au_n nanoparticles with $17 \leq n \leq 58$, and reached an average RMSE of 9 meV/atom for energies [27]. Jindal *et al.* trained an ANN potential with

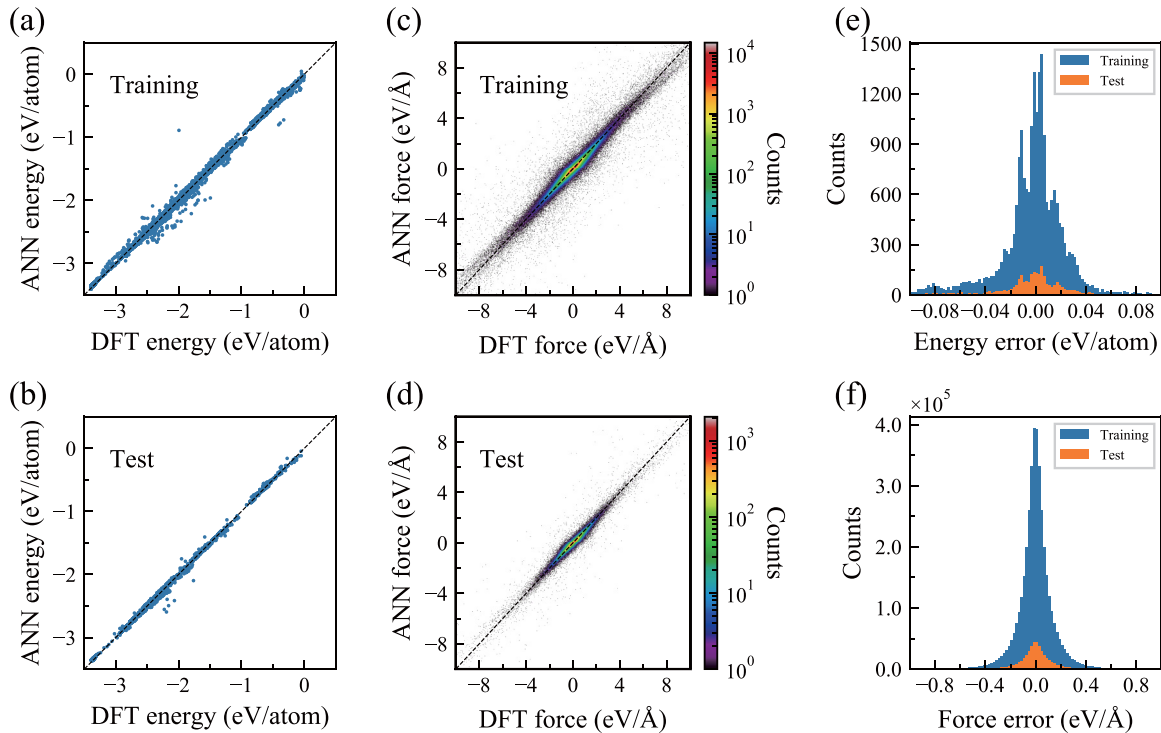


FIG. 1. Comparisons of the ANN results with respect to the references calculated by DFT. (a) and (b) show the comparisons of energies per atom for training and test set, respectively. (c) and (d) exhibit force correlations for training and test set, 2D histogram plots are adopted to illustrate the density distribution of errors. To highlight the main part of the force comparisons, the ranges shown here are limited from -10 to 10 eV/Å, still, 99.93% of the statistical data in the training set and 99.94% of the test data are included. (e) and (f) display the error distributions for energies and forces, blue bars denote the training set, and orange bars represent the test set.

an RMSE of 5 meV/atom by fitting the PES of Au_{30} – Au_{147} clusters [72]. Restricting training samples to specific types of structures can greatly improve accuracy. As another example of Au clusters, Ouyang and co-workers developed a neural network potential specifically for Au_{58} , the RMSE for the training set was only 0.60 meV/atom [71]. Such a small error was obtained because the number of Au atoms in the training set was fixed at 58, meanwhile, the obtained potential was limited to deal with Au_{58} only. On the contrary, increasing the diversity of samples may cause a decrease in accuracy. The ANN potential trained for 55-atom Ag–Au nanoalloys [30], as well as the ANN potential developed for icosahedral Pt–Cu–Ni nanoparticles with 147, 309 and 561 atoms [75] have both reached the accuracy within 10 meV/atom. However, for the ANN potential of the Cu–Pd–Ag trimetallic system using nonequilibrium bulk structures, clusters with 30–80 atoms and alloys with 55 atoms as training samples, although the overall RMSE of energies reached 3–10 meV/atom, the error when dealing with cluster structures was around 12–16 meV/atom [76]. In our work, as described in the sampling section, our training set contained bulk and cluster structures of different types, sizes and hydrogen content. In order to increase the versatility of our ANN potential, we have greatly enriched the diversity of our training samples, which may lead to a reduction in accuracy.

In addition, we noticed that for the ANN potential of Au_{58} developed by Ouyang [71], the energy span of the training samples was 0.17 eV/atom, another potential trained for Na clusters by Chiriki *et al.* used samples with energy span of

0.21 eV/atom from the lowest energy structure [26]. For our case, the energy span in the training set was nearly 3.5 eV/atom, which was much larger than reported above. A comparable situation was reported in Ref. [64], where Deringer *et al.* constructed a ML potential for amorphous carbon. The energy span in their training samples was about 3 eV/atom, and their RMSEs of energies were in the range of tens of meV/atom, which was similar to our results.

Most previously developed ML potentials were not designed to be universal for simulating all kinds of structures, but our aim in this work was to try to improve the versatility of our Mg–H ANN potential as much as possible to make it suitable for different types of structures and simulation processes. The validations and calculations in the following sections will prove that our potential is capable of dealing with magnesium hydride bulks and clusters of different sizes and hydrogen content, capable of capturing the diffusion of H atoms on the surface or inside of magnesium hydrides, and even capable of simulating the gaseous H_2 systems and computing the dissociation of H_2 on the surface of Mg. Therefore we believe a certain sacrifice in accuracy is acceptable here. Moreover, the error of force in our calculation has reached the typical standard.

D. Computational details

All DFT calculations were performed using Vienna ab initio simulation package (VASP) [79] within the projector-augmented-wave (PAW) approach [80]. The

Perdew-Burke-Ernzerhof (PBE) exchange-correlation functional within the generalized gradient approximation (GGA) [81] was adopted for all the computations, and a plane-wave cutoff energy of 500 eV was used. The self-consistent field (SCF) convergence criterion was set to be 10^{-5} eV for the total energy change, and the convergence threshold for local optimization was set at 0.02 eV/Å for the maximum force on atoms. Samples of nanoclusters were located in cubic simulation boxes, vacuum spaces of at least 10 Å were applied in all three directions to prevent interactions between periodic images. The van der Waals interactions were not included in the calculation of training samples, because Morawietz *et al.* have concluded that for situations involving intermolecular interactions, the van der Waals corrections can be added directly to the ML potential derived from plain GGA-PBE results [82]. In the subsequent sections, we used Grimme's DFT-D3 method [83,84] in the simulation of H-H interactions and H₂ dissociation PES on Mg(0001) surface where van der Waals corrections were required.

An in-house modified version of TENSORMOL program [85] was utilized to construct the machine-learning potential. This modified TENSORMOL code was connected to the atomic simulation environment (ASE) framework [86,87] as a computing module, through which structural optimization and MD simulations based on the ANN potential can be achieved. Phonon dispersion was calculated using the finite displacement method interfaced with the PHONOPY code [88,89]. The effects of van der Waals interactions on energies and forces were implemented in conjunction with Grimme's DFTD3 program through ASE framework.

III. VALIDATION

A. Bulk properties

Basic bulk properties calculated from our ANN potential and DFT are listed in Table II, including lattice parameters, cohesive energies and bulk moduli. Meanwhile, previously reported experimental data and theoretical results are also listed for comparison. Except for the cohesive energy of β -MgH₂, for all the MgH₂ and Mg crystals considered, the lattice parameters and cohesive energies calculated by ANN potential are in good agreement with those obtained from our DFT calculations as well as those reported [90–93]. Based on the cohesive energies calculated by ANN, α -MgH₂ and hcp-Mg are the most stable crystalline forms, respectively, which is consistent with the experimental observations. There is a relatively large deviation of 66 meV/atom when calculating the cohesive energy of β -MgH₂. It was found that the sample with lowest overall energy show the lowest fitting error in the previous training of ML potential [64]. Due to the high overall energy of β -MgH₂, a large fitting error occurs. However, since β -MgH₂ only exists under high pressure, the transition pressure from α -MgH₂ to β -MgH₂ is as high as 9.7 GPa [94], so β -MgH₂ will not appear in general simulation conditions. Therefore the large error in the calculation of β -MgH₂ cohesive energy does not affect the performance of our ANN potential in the subsequent simulations.

TABLE II. Comparison of lattice parameters (a_0 , b_0 , and c_0), cohesive energies (E_{coh}) and bulk moduli (B) of various crystal structures of MgH₂ and Mg calculated from ANN, DFT, or obtained from previous reports. Values in the second column are calculated using our ANN potential, the third column shows our DFT calculation results, and the forth column lists some experimental and theoretical results.

Properties	ANN	DFT	References
α -MgH ₂			
a_0 (Å)	4.511	4.509	4.485 ^a , 4.517 ^c
c_0 (Å)	3.042	3.012	2.999 ^a , 3.021 ^c
E_{coh} (eV/f.u.)	-6.580	-6.595	-6.676 ^d
B (GPa)	53.837	52.712	51 ^a , 51.963 ^b , 45 ± 2 ^c
β -MgH ₂			
a_0 (Å)	4.743	4.741	4.790 ^a , 4.666 ^c
E_{coh} (eV/f.u.)	-6.463	-6.265	-6.348 ^d
B (GPa)	62.575	60.840	56 ^a , 56.260 ^b , 47.41 ± 4 ^c
γ -MgH ₂			
a_0 (Å)	4.540	4.500	4.486 ^a , 4.525 ^c
b_0 (Å)	4.953	4.901	4.898 ^a , 4.928 ^c
c_0 (Å)	5.407	5.410	5.402 ^a , 5.444 ^c
E_{coh} (eV/f.u.)	-6.574	-6.592	-6.675 ^d
B (GPa)	55.969	53.558	48 ^a , 47.833 ^b , 44.0 ± 2 ^c
hcp-Mg			
a_0 (Å)	3.161	3.163	3.184 ^d
c_0 (Å)	5.152	5.268	5.249 ^d
E_{coh} (eV/f.u.)	-1.505	-1.499	-1.593 ^d
B (GPa)	42.723	35.139	37 ^d
fcc-Mg			
a_0 (Å)	4.467	4.518	4.506 ^d
E_{coh} (eV/f.u.)	-1.505	-1.490	-1.481 ^d
B (GPa)	42.705	34.566	–
bcc-Mg			
a_0 (Å)	3.550	3.581	3.579 ^d
E_{coh} (eV/f.u.)	-1.490	-1.471	-1.564 ^d
B (GPa)	45.724	34.191	36 ^d

^aTheoretical value from Ref. [90].

^bTheoretical value from Ref. [91].

^cExperimental value from Ref. [92].

^dTheoretical value from Ref. [93], available online at Materials Project (<https://www.materialsproject.org>).

Bulk moduli were obtained by fitting the Birch-Murnaghan equation of state (EOS) [95–97]. It is known that the PBE functional overestimates the value of bulk modulus, which gives an explanation for the calculated value of ANN being larger than the experiments. Nevertheless, the bulk modulus of MgH₂ calculated by ANN can perfectly reproduce the DFT results, which is enough to validate the accuracy of our ANN potential.

All atomic environments required to calculate the listed properties for MgH₂ and hcp-Mg crystals are covered in the

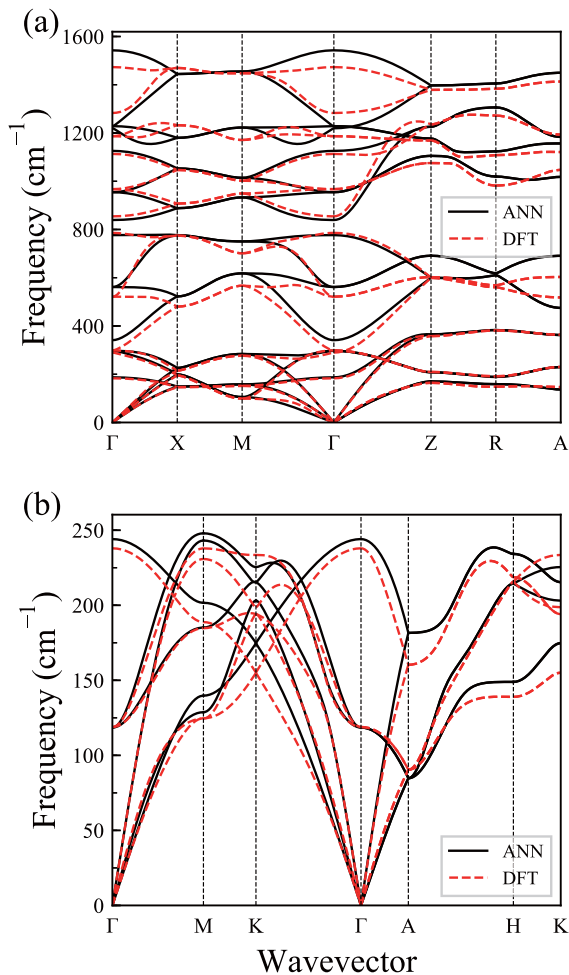


FIG. 2. Phonon dispersions calculated by ANN potential (black solid lines) and DFT (red dashed lines) for (a) α -MgH₂ and (b) hcp-Mg.

training data through our sampling strategy, which guarantees its consistency with the DFT results. Interestingly, the face-centered cubic (fcc) fcc-Mg and body-centered cubic (bcc) bcc-Mg structures were not included in the training samples, their bulk properties calculated by ANN, however, are still similar to DFT values. This further proves the flexibility and universality of the ANN potential we have trained.

B. Phonon dispersion

The capability of a potential to describe the lattice dynamics depends on the accuracy of calculating the forces acting on atoms. Because of the sensitivity to the change of force, phonon dispersion has become a good method for evaluating force calculations. We employed the finite displacement method as implemented in PHONOPY [88,89] to calculate phonon dispersions for α -MgH₂ and hcp-Mg crystals. Same models and settings were used in ANN and DFT calculations where $3 \times 3 \times 3$ supercells were adopted containing 162 atoms for α -MgH₂ and 54 atoms for hcp-Mg, respectively, and the displacement distance was set to 0.01 Å. Figure 2 illustrates the phonon dispersion for α -MgH₂ and hcp-Mg, making comparisons between ANN and DFT results.

The high-symmetry points were chosen according to Refs. [98,99].

Overall, the phonon dispersions obtained with the machine-learning potential reproduce the DFT results well. For α -MgH₂ shown in Fig. 2(a), the acoustic modes calculated by the two methods are perfectly overlapped, with only small disagreements present for some optical modes. The optical modes are related to the electric dipole moments of the ions in the crystal, note that the atomic charges are not considered in our machine-learning potential model, which may causes the small discrepancies. Moreover, no mode with imaginary frequency is detected from ANN calculations for both structures, which is in consistent with the stability of the two crystals.

C. H-H interactions

Through comparing bulk properties and phonon dispersions, the accuracy of our machine-learning potential for Mg-H and Mg-Mg interactions are validated. We next examine the ability of the potential to handle H-H interactions. Hydrogen exists in gaseous form at room temperature, in this situation the methods mentioned above for bulk systems are no longer adequate. We chose a method used by Zhou *et al.* in Ref. [100], performing MD simulations on an artificially built crystalline form of hydrogen to observe the evolution of its structure. First, 1000 hydrogen atoms were constructed in a diamond-cubic crystal structure, as shown in Fig. 3(a), with the H-H distance of 1.359 Å, placed in the center of a periodic cubic simulation box with a side length of 50 Å. MD simulation was then carried out at a temperature of 300 K with a timestep of 1 fs. Since we expected it to be a gaseous state, van der Waals correction using DFT-D3 method was applied during the simulation to properly account for the intermolecular interactions. As a result, the crystalline structure fell apart from the beginning of the simulation, with hydrogen atoms paired up to form H₂ molecules. A snapshot of the system after 20 ps of simulation is demonstrated in Fig. 3(b), from which we can clearly see the gaseous behavior of the hydrogen that 97.0% of the atoms are in the molecular H₂ form, and are spread out in the space. Figure 3(c) plots the per-frame averaged distribution of H-H distances in the MD trajectory of the last 5 ps, most of which are in the range of 0.7 to 0.8 Å, well-reproduce the equilibrium bond length of H₂ molecule at 300 K. By the way, without DFT-D3 correction, we still observed the gaseous behavior of H₂, and got almost identical distribution of H-H distances. The results prove that our machine-learning potential is suitable for computing H₂ molecules and gaseous hydrogen systems. Moreover, it provides the possibility for simulation under hydrogen atmosphere and calculation of surface hydrogen adsorption.

D. H₂ dissociation PES on Mg(0001) surface

As a hydrogen storage material, the dissociative adsorption of H₂ at the surface is an important subject to study. To this end, the ANN is expected to predict potential energies in the reactive channel. It is not our original intention here to design a machine-learning potential for surface reactions, we therefore did not create reference samples related to the breaking of chemical bonds on purpose. Nevertheless, with the help

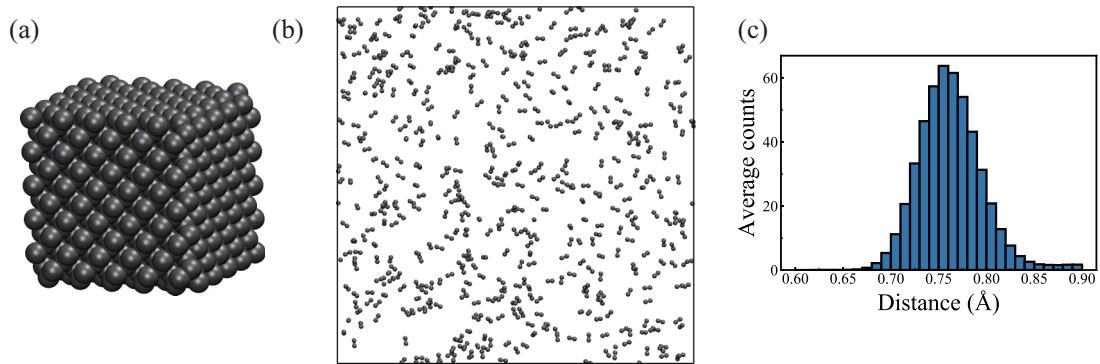


FIG. 3. (a) Initial diamond-cubic crystal structures of 1000 hydrogen atoms. (b) Snapshot of the final structure after 20 ps MD simulation at 300 K. (c) The per-frame averaged distribution of H-H distances in the MD trajectory of the last 5 ps.

of high-temperature MD simulation and adaptive sampling strategy, samples containing information on the dissociation of hydrogen molecules were automatically generated, which prompted us to study the performance of our ANN in characterizing the H_2 dissociation PES on Mg surface.

As shown in Fig. 4, Mg(0001) surface is modeled using a four-layer slab in a 4×4 supercell, an additional 20 Å vacuum space is placed in the Z-direction between slabs to avoid layer-to-layer interactions. All Mg atoms are held fixed during the PES calculation, and hydrogen atom pairs with

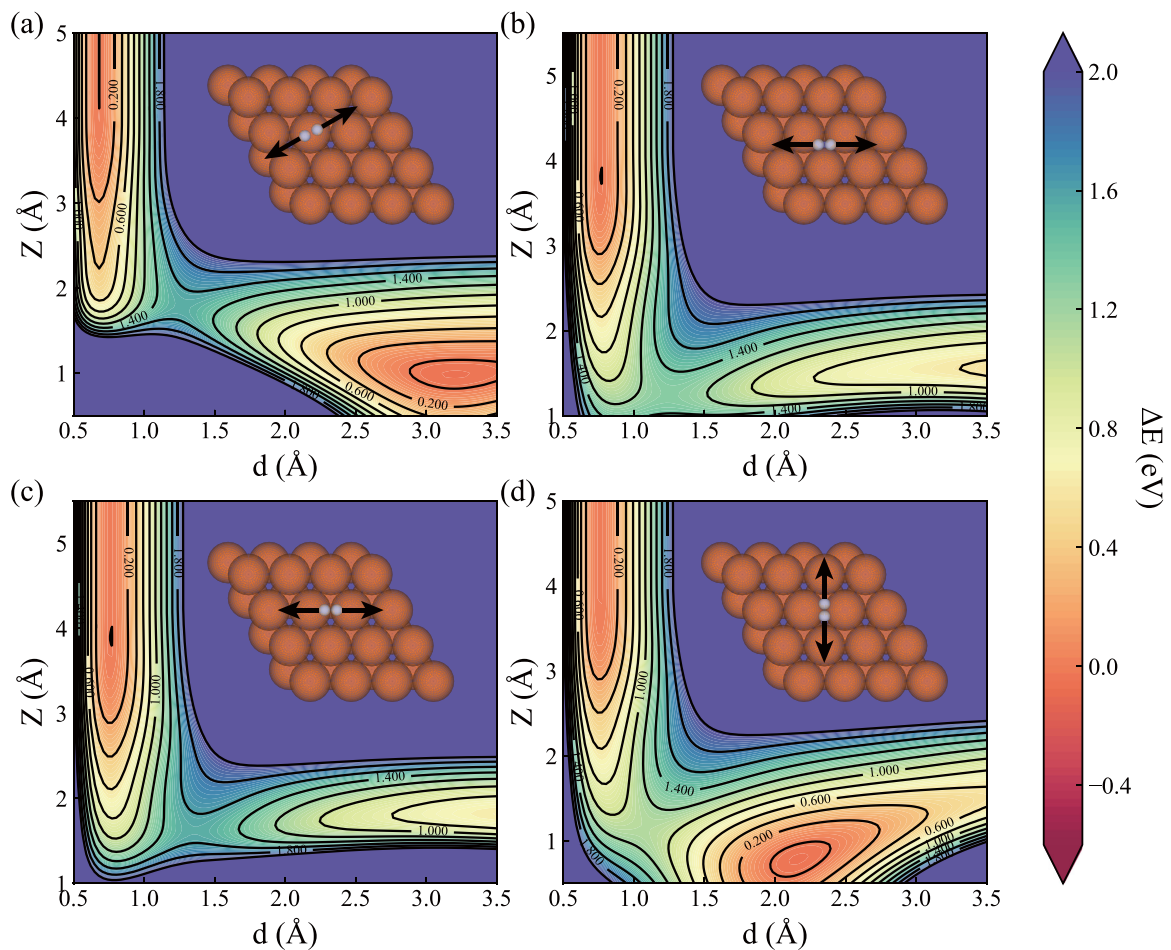


FIG. 4. Two-dimensional contour plots of the machine-learning PES as a function of Z and d , where Z is the vertical distance of the H_2 molecule above the frozen Mg(0001) surface, d is the distance between two H atoms. (a) H_2 center of mass fixed at top site, H atoms moving toward hcp and fcc hollow sites; (b) H_2 center of mass fixed at fcc hollow site, H atoms moving toward adjacent hcp hollow sites; (c) H_2 center of mass fixed at bridge site, H atoms moving toward adjacent top sites; (d) H_2 center of mass fixed at bridge site, H atoms moving toward adjacent hcp and fcc hollow sites. Orange balls denote Mg atoms, white balls denote H atoms, black arrows indicate the directions in which hydrogen atoms are moving.

different H-H distances approach the surface from different sites. There are four types of high-symmetry sites on the Mg(0001) surface, which are top site, bridge site, hcp hollow site, and fcc hollow site. Since our purpose is to verify the performance of our ANN potential, we have made some simplifications. Hydrogen atom pairs are all kept parallel to the surface, with their center of mass fixed at top site as shown in Fig. 4(a), fixed at fcc hollow site as shown in Fig. 4(b), and fixed at bridge site as shown in Figs. 4(c) and 4(d), the directions in which the hydrogen atoms are separated from each other are indicated by arrows.

The results show that hydrogen prefers to dissociate at the bridge site, and move towards two neighboring hollow sites (one hcp site, and one fcc site), as shown in Fig. 4(d). Under this condition, the activation energy is 1.12 eV, which is consistent with previously reported 1.15 eV [101] calculated by DFT using the RPBE exchange-correlation functional [102] within the GGA. The hydrogen pair in the transition state is 1.15 Å above the Mg(0001) surface with a H-H bond length of 1.08 Å, also similar to the reported values calculated using the GGA-PBE functional [103]. In addition, studies have shown that the configuration with two separated hydrogen atoms occupying adjacent hcp and fcc hollow sites is not the most stable one, H atom can easily move from an hcp site to an fcc site [101,103]. To this end, we first optimized the surface adsorption model with two H atoms in neighboring hcp and fcc sites, then optimized the structure with two H atoms in two nearest fcc sites, comparison of the two models shows that the energy of the latter is 0.134 eV lower than the former, which is also in good agreement with the previous calculation [101].

It should be noted that during the H₂ adsorption and dissociation processes, the van der Waals interaction between H₂ molecule and the surface of Mg has an influence on the calculation. However, in this article, the purpose of calculating the H₂ dissociation PES is to verify the accuracy of our ANN potential. Since the reference values in the literature were calculated by GGA-PBE and GGA-RPBE methods without considering the van der Waals correction, we did not add van der Waals correction in the above calculations. In fact, van der Waals interaction will have a certain impact on the energy of the dissociation process. After adding DFT-D3 correction to the ANN calculation, the contour of the PES does not change much. The dissociation of H₂ still prefers to occur at the bridge site as shown in Fig. 4(d), and move towards two neighboring hollow sites. In the transition state of bridge-site dissociation, the hydrogen pair is still 1.15 Å above the Mg(0001) surface, and the H-H distance is 1.07 Å, which are almost the same as the results without DFT-D3 correction. As for the activation energy, after adding DFT-D3 correction, the activation energy of the bridge-site dissociation is 1.00 eV, which is 0.12 eV lower than that without DFT-D3 correction. From the perspective of verifying the potential, the above calculations show that our ANN potential can describe the surface dissociation of H₂. At the same time, by comparing the results before and after van der Waals correction, it can be seen that our ANN potential is capable of considering the intermolecular interactions by combining with the DFT-D3 method when calculating weakly bound systems.

Although other variables such as H₂ molecular tilt angle on the Mg(0001) surface are not considered when characterizing PES, this calculation proves that our ANN potential can deal with the surface H₂ dissociation.

IV. APPLICATIONS

A. MD simulations

In order to understand the effect of cluster size, temperature and composition on the structural properties and hydrogen diffusion properties of magnesium hydride clusters, we performed canonical MD simulations on clusters with diameters ranging from 1.6 to 4.0 nm using our machine-learning potential. Four different sizes of magnesium hydride clusters were considered, with diameters of 1.6, 2.4, 3.0, and 4.0 nm, containing 80, 248, 458, and 1098 Mg atoms, respectively. For each size of the cluster, we studied four different compositions with $(N_{\text{Mg}} : N_{\text{H}}) = (2 : 1), (1 : 1), (2 : 3),$ and $(1 : 2)$, where N_{Mg} and N_{H} represent numbers of Mg and H atoms, respectively. Hydrogen diffusion was simulated at five different temperatures, ranging from 300 to 700 K with an interval of 100 K. The initial atomic configurations of Mg_nH_{2n} ($n = 80, 248, 458, 1098$) clusters were generated by cutting out spheres from α -MgH₂ crystal lattice, and the initial structures of Mg_nH_m clusters with $m < 2n$ were obtained by randomly removing part of the hydrogen atoms from the corresponding Mg_nH_{2n} clusters. In all cases, the starting configurations were firstly relaxed for 0.2 ns at 700 K using the NVT ensemble, and then gradually cooled to 300 K in 0.4 ns to get the well-equilibrated structures. For each temperature considered, a further equilibration of 0.1 ns was performed, followed by another 0.1 ns simulations to produce MD trajectories for subsequent analysis. The time step was 1.0 fs for each step, and the temperature was controlled using the Langevin thermostats [104]. During our MD simulations, since the dissociation of H₂ and the decomposition of clusters never occurred, the influence of the intermolecular interaction was very small, so van der Waals correction was not added in the calculation. Nevertheless, we still tested and compared the simulation results with or without DFT-D3 correction, and found that considering the van der Waals interaction did not change the qualitative picture of the simulation, and all subsequent research conclusions remained the same, which further proved the rationality of our calculations.

B. Mg_nH_{2n} clusters

The snapshots of MD equilibrated geometries of Mg_nH_{2n} ($n = 80, 248, 458, 1098$) nanoclusters at 300 K are shown in Fig. 5. With this stoichiometric composition, the Mg_nH_{2n} clusters are approximately spherical, with no hydrogen molecules formed and released during the MD processes. Hydrogen atoms on the surface of the clusters prefer to bond to two Mg atoms, rather than occupying the fcc hollow sites adjacent to three Mg atoms on the Mg(0001) surface. This is consistent with the conclusions drawn in our previous research that hydrogen atoms tend to occupy two-fold coordinated bridge sites on the surface of Mg₅₅ clusters [105]. To explore the atomic local structure in the core region of clusters, we calculated the average coordination numbers (CNs) of Mg and H atoms, the last 50 000 MD trajectories at 300 K for each

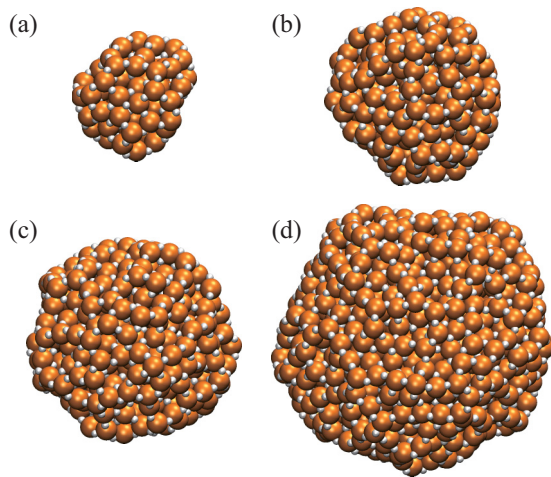


FIG. 5. Equilibrated geometries of Mg_nH_{2n} nanoclusters at 300 K after 0.1 ns MD simulations. (a) $Mg_{80}H_{160}$, (b) $Mg_{248}H_{496}$, (c) $Mg_{458}H_{916}$, and (d) $Mg_{1098}H_{2196}$. Orange balls represent Mg atoms, white balls represent H atoms.

cluster were taken into account. For the four Mg_nH_{2n} clusters studied, the Mg coordination numbers for H atoms inside the clusters are in the range of 3.22 to 3.26, and the H coordination numbers for Mg atoms inside the clusters are in the range of 6.02 to 6.32, indicating that most of the internal H atoms are bonded to three Mg atoms, a small part is bonded to four Mg atoms, and the Mg atoms inside the clusters tend to be bonded to six H atoms. From the perspective of CN, these values are similar to the case of threefold coordination of H atoms and sixfold coordination of Mg atoms in α - MgH_2 , yet significant deformation can be seen in the equilibrated structures.

To further study the structural characteristics, we calculated the radial distribution functions (RDFs) of Mg_nH_{2n} clusters. The RDFs of $Mg_{1098}H_{2196}$ at 300 K are shown in Fig. 6, together with the RDFs for the crystals of α - MgH_2 at 300 and 600 K for comparison. It should be pointed out that size dependence is not detected in the RDF curves of four considered Mg_nH_{2n} clusters, so here we take $Mg_{1098}H_{2196}$ as a representative to discuss the structural properties. In Fig. 6(a), for Mg-Mg pairs, the doublet peaks positioned in the range of 2.8 to 4.0 Å for α - MgH_2 crystal are degenerated into a broad single peak for $Mg_{1098}H_{2196}$, and the peaks beyond 4.0 Å are almost vanished for the cluster. In Fig. 6(b), the vanishing of peaks beyond 2.9 Å in the Mg-H partial RDFs of $Mg_{1098}H_{2196}$ is also observed. All these changes indicate that in the magnesium hydride clusters with a diameter of less than 4 nm at 300 K, the atoms are arranged in a liquid-like disordered manner. Nevertheless, as shown in Fig. 6(c), in the case of H-H partial RDFs, although the peaks for cluster are still degenerated compared to the MgH_2 crystal, they catch some features of the crystal RDF, such as the small peak at 3.9 Å, and the shape of the curve for $Mg_{1098}H_{2196}$ cluster within 6.0 Å is almost identical with that of the α - MgH_2 crystal at 600 K. Combined with the results of CN discussed above, it can be found that the hydrogen atoms retain the bonding style in the α - MgH_2 crystal to a certain extent.

Figure 7 demonstrates the temperature dependence of H-H partial RDFs of $Mg_{1098}H_{2196}$ cluster. As the temperature

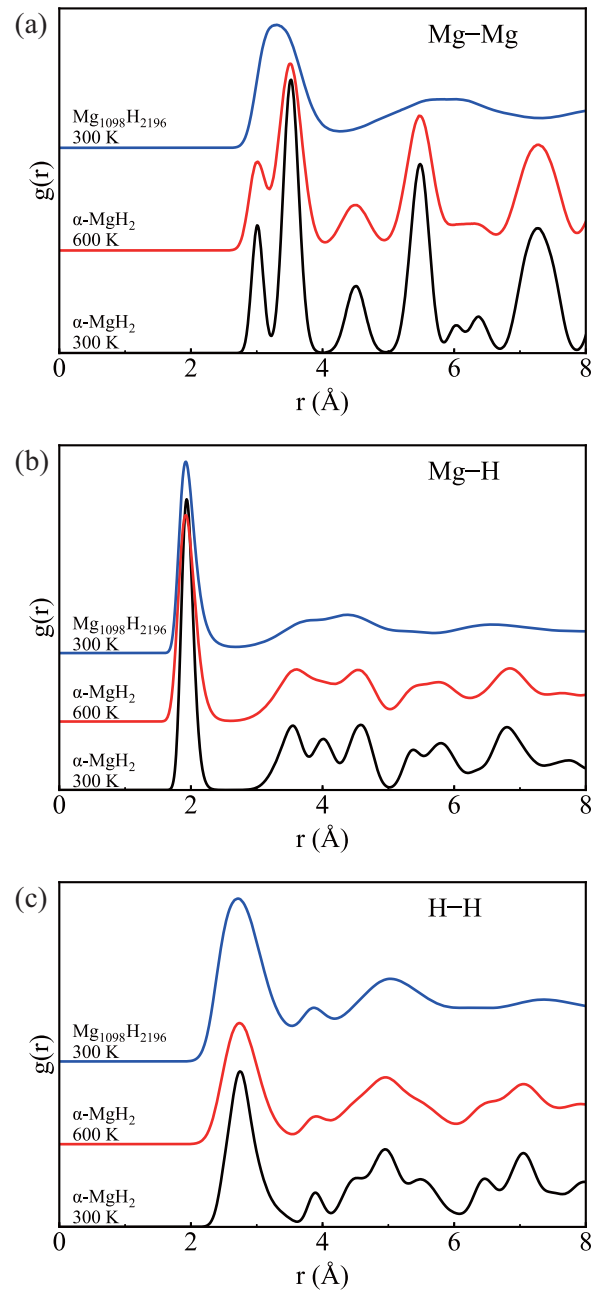


FIG. 6. Comparison of the radial distribution functions (RDFs) of $Mg_{1098}H_{2196}$ at 300 K and RDFs for the crystal of α - MgH_2 at 300 and 600 K. (a) The Mg-Mg partial RDFs, (b) the Mg-H partial RDFs, (c) the H-H partial RDFs. Blue lines denote $Mg_{1098}H_{2196}$ cluster at 300 K, red lines denote α - MgH_2 at 600 K, and black lines denote α - MgH_2 at 300 K.

increases from 300 to 700 K, the small peak at 3.9 Å gradually disappears, and other peaks also widen and flatten. This result further confirms the existence of short-range order in low-temperature Mg_nH_{2n} clusters.

C. Mg_nH_m ($m < 2n$) clusters

The snapshots of MD equilibrated geometries of Mg_nH_m ($m = n/2, n, 3n/2$) nanoclusters at 300 K are shown in Fig. 8. Here we use balls to show the Mg atoms that are not bonded to H atoms, and use sticks representing Mg-H bonds to show the

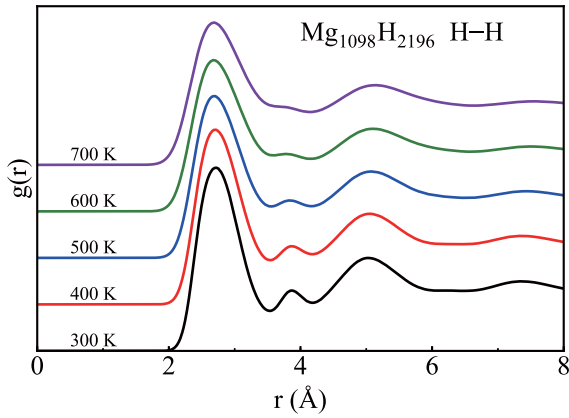


FIG. 7. The temperature dependence of H-H partial RDFs of $\text{Mg}_{1098}\text{H}_{2196}$ cluster.

hydrogenated parts of the clusters. This way, the segregation of Mg phase and MgH_x phase is clearly seen for each cluster. Since the MD initial structures of these clusters were generated by randomly removing H atoms from Mg_nH_{2n} clusters, at beginning the remaining H atoms were randomly distributed in the clusters, after MD processes, Mg atoms aggregated spontaneously, forming Mg clusters without H atoms inside.

Except that H atoms in $\text{Mg}_{80}\text{H}_{40}$ and $\text{Mg}_{248}\text{H}_{124}$ are abundant on the surface of the Mg part due to the small number, H atoms in other clusters mainly exist in the MgH_x part. It is found that the Mg : H atomic ratio in MgH_x part of each cluster is approximately 1 : 2, and this part of the cluster has the same structural characteristics as Mg_nH_{2n} . In this subsection, we mainly focus on the Mg part of the cluster. As can be seen from Fig. 8, in the Mg part of the $\text{Mg}_{1098}\text{H}_{548}$ and $\text{Mg}_{1098}\text{H}_{1098}$ clusters, Mg atoms exist in an ordered manner. To confirm this observation, we calculated Mg-Mg RDFs for atoms in the Mg part of each cluster, and some representative results are shown in Fig. 9.

For Mg_nH_n clusters simulated at 300 K, Fig. 9(a) shows the size dependence of structural order in the Mg phase. The Mg-Mg partial RDF of hcp-Mg crystal is plotted in black at the bottom. As the cluster size increases, the size of the corresponding Mg phase also becomes larger, and more peaks appear in the RDF curve. Except for the single peak locating at 3.2 Å, no significant peaks are observed for $\text{Mg}_{80}\text{H}_{80}$ and $\text{Mg}_{248}\text{H}_{248}$ clusters. In $\text{Mg}_{458}\text{H}_{458}$, signal appears near 4.5 Å, and a tendency of double peaks can be seen in the range of 5.0 to 6.8 Å. When the cluster size is up to $\text{Mg}_{1098}\text{H}_{1098}$, more intense peaks appear, and it reproduces the RDF curve of hcp-Mg crystal very well. The peak showing the second nearest neighboring Mg atoms at 4.5 Å and the doublet peaks between 5.0 and 6.8 Å are almost identical to those in hcp-Mg. Obviously, with the increase of the cluster size, the structural ordering of the Mg phase increases significantly, and the nanocrystalline structure is clearly detected when the average diameter of the Mg part of the cluster reaches about 2.5 nm as in $\text{Mg}_{1098}\text{H}_{1098}$.

Another factor affecting the structure of the Mg phase is temperature. The Mg-Mg partial RDF curves of the Mg phase in the $\text{Mg}_{1098}\text{H}_{1098}$ cluster at different temperatures are compared in Fig. 9(b). Similarly, the RDF curve of hcp-Mg crystal

at 300 K is plotted at the bottom for reference. Below 500 K, the RDF curves of the clusters basically match the curve of hcp-Mg crystal. As the temperature increases, the outline of the RDF curve becomes smoother, and the peak representing the second nearest neighboring Mg atoms at 4.5 Å gradually disappears, also the doublet peaks between 5.0 and 6.8 Å degenerate to a single broad peak, and the two peaks between 6.8 and 8.0 Å are flattened. When it reaches 700 K, all the peaks beyond 4.0 Å basically disappear, and the Mg phase adopts a liquidlike structure.

With the help of RDF, it is possible to distinguish clusters with crystalline and liquid-like structures. To further determine the type of crystal structures for solid-like clusters, the Steinhardt bond-orientational order (BOO) parameters [106] are employed. For atom i , the vector $q_{lm}(i)$ is defined as

$$q_{lm}(i) = \frac{1}{N_i} \sum_0^{N_i} Y_{lm}(\theta(r_{ij}), \phi(r_{ij})), \quad (9)$$

where the $Y_{lm}(\theta(r_{ij}), \phi(r_{ij}))$ are spherical harmonics, l is an integer with $l \geq 0$, m is an integer with $-l \leq m \leq l$, N_i is the number of bonds of atom i . To improve the accuracy of structure discrimination, the averaged form of the local BOO parameters proposed by Lechner and Dellago [107] is introduced:

$$Q_{lm}(i) = \frac{1}{N_i + 1} \left(q_{lm}(i) + \sum_{j=0}^{N_i} q_{lm}(j) \right), \quad (10)$$

where the sum of q_{lm} over all neighbors of central atom i plus the atom i itself are considered, and therefore contains the structural information of the second shell of neighboring atoms. In this work, the BOO parameters were calculated using the PYBOO code developed by Leocmach [108], the detailed description of the algorithm can be found in Ref. [109].

The BOO parameters are sensitive to different types of crystals with different values of l . For Mg phase in the Mg_nH_n clusters, $l = 4$ and 6 are chosen. Figure 10 shows the correlation maps of Q_4 - Q_6 for different sizes of Mg_nH_n clusters at 300 K. The BOO parameters for perfect crystal structures are pointed out with their names, the (Q_4, Q_6) pairs for hcp, fcc and bcc crystals are (0.0972, 0.4848), (0.1909, 0.5745), and (0.0364, 0.5107), respectively. For small clusters like $\text{Mg}_{80}\text{H}_{80}$, the Q_6 parameter for each atom is smaller than 0.3. A larger value of BOO parameter indicates higher ordering of the local atomic structure. From Fig. 10(a), the BOO parameters for atoms in both Mg phase and MgH_x phase are very small, indicating that there is no obvious order in the small clusters at 300 K. For $\text{Mg}_{248}\text{H}_{248}$ as shown in Fig. 10(b), Q_6 values are getting larger, and some atoms are classified as surface atoms. Note that through the BOO calculations, a bond can be determined as either crystalline or noncrystalline, and the type of an atom is then classified according to the number of crystalline bonds it has. An atom needs to have at least 10 crystalline bonds to be identified as a crystal atom, one with 4 to 9 crystalline bonds is considered a surface atom. The results shown in Fig. 10(b) reveal an increasing trend of the structure ordering. In Figs. 10(c) and 10(d), more atoms have higher values of Q_6 , for $\text{Mg}_{1098}\text{H}_{1098}$, noticeable portion of crystal atoms are detected, indicating the existence of a highly

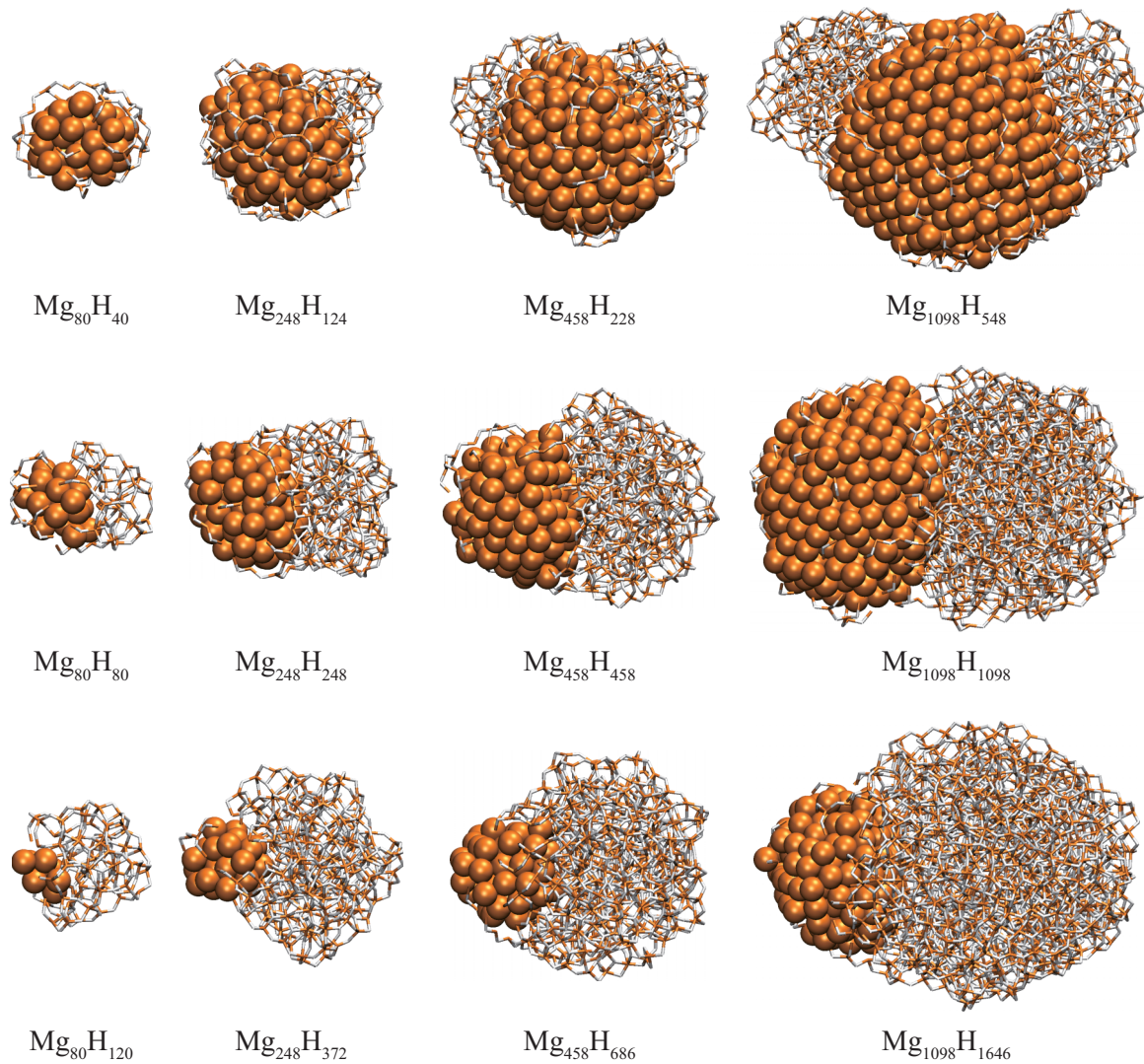


FIG. 8. Equilibrated geometries of Mg_nH_m ($m < 2n$) nanoclusters at 300 K after 0.1 ns MD simulations. Orange balls represent Mg atoms that are not bonded to H atoms, and sticks represent Mg-H bonds, where the end near the Mg atom is orange and the end near the H atom is white.

ordered crystalline structure. Combining with the models of the cluster demonstrated in Figs. 10(e) and 10(f), the MgH_x part still shows no ordering, but the Mg part of the cluster has a nanocrystalline structure, which is consistent with the RDF results. A clear boundary can be seen between the two phases of Mg and MgH_x . Figure 10(d) shows that most of the ordered Mg atoms have the signature of hcp crystal structure, and a small part of Mg atoms have the characteristics of fcc structure.

Next, the effect of temperature on the cluster structure is shown in Fig. 11. When the temperature increases to 400 or 500 K, the distribution of atomic BOO parameters in the Q_4 - Q_6 correlation map does not change much compared to 300 K, and the Mg phase retains nanocrystalline structure. Continue to increase the temperature to 600 K, the number of atoms with crystal characteristics decreases, although the Mg phase is still recognized as an hcp-type nanocrystal, the disordered features gradually emerge, which are consistent with the results shown by the aforementioned RDF analysis. Finally at 700 K, the Q_6 values of atoms in the Mg phase decrease, and

the crystalline structure disappears completely, with both Mg and MgH_x phases showing liquid-like structures.

Approximately, the effect of atomic composition on the structure of clusters and the effect of size are related. The order of the cluster structure in the Mg phase is mainly affected by the size of the Mg side of the cluster. Because of phase separation, for clusters with the same number of Mg atoms, the size of the Mg phase is larger in clusters containing fewer H atoms. As shown in Fig. 12, for $Mg_{1098}H_m$, as the number of hydrogen atoms decreases, the number of crystalline atoms increases, and the degree of structural ordering improves.

The nucleation and growth of Mg have been observed for bulk and nanocrystalline MgH_2 in the experiments [110,111]. Although the growth of Mg cluster was not detected in the beginning of the dehydrogenation process reported by Gan-grade and co-workers [111], due to the high vapor pressure of Mg, the sintering and growth of the Mg nanocrystallites is expected to happen over time, leading to a segregated structure similar to our modeled case. Furthermore, it has been found in experiments that high-density grain boundaries in clusters can

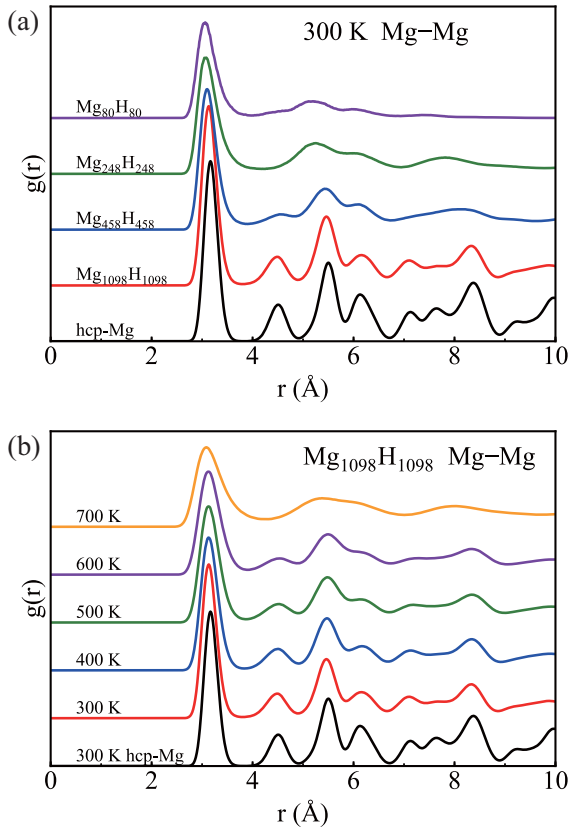


FIG. 9. (a) The Mg-Mg partial RDFs for atoms in the Mg part of different size of Mg_nH_n clusters at 300 K. (b) The Mg-Mg partial RDFs for atoms in the Mg part of $Mg_{1098}H_{1098}$ cluster at different temperatures. The Mg-Mg partial RDF of hcp-Mg crystal is plotted in black at the bottom of each panel for comparison.

improve the hydrogen storage kinetics of Mg [112], because H atoms diffuse mainly through the grain boundaries between Mg and MgH_2 , or through the interfaces or defects inside the hydride phase [113]. In this study, the calculated phase separation of the clusters and crystallization of the Mg phase theoretically support the experimental conclusions above.

D. Diffusion coefficient

Poor hydrogen absorption and desorption kinetics are major bottlenecks in restricting the practical application of MgH_2 . The diffusion rate of hydrogen in Mg and MgH_2 is an important factor affecting the hydrogen absorption and desorption performance. To evaluate the diffusion properties of hydrogen atoms in the clusters, we calculated the diffusion coefficients (D) of hydrogen atoms in magnesium hydride clusters of different sizes and compositions at different temperatures.

Trajectories from the last 0.1 ns MD simulation were used to calculate the mean-squared displacement (MSD) of hydrogen atoms in the clusters. The MSD is defined as

$$\begin{aligned} \text{MSD}(t) &= \langle [\mathbf{r}(t_0 + t) - \mathbf{r}(t_0)]^2 \rangle \\ &= \frac{1}{NM} \sum_{i=1}^N \sum_{j=1}^M [\mathbf{r}_i(t_j + t) - \mathbf{r}_i(t_j)]^2, \end{aligned} \quad (11)$$

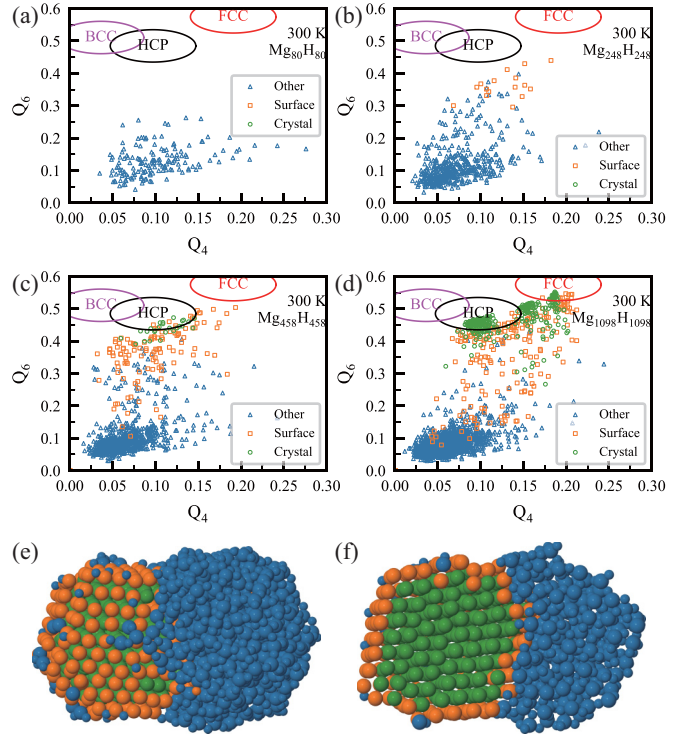


FIG. 10. Correlation maps of BOO parameters Q_4 - Q_6 for (a) $Mg_{80}H_{80}$, (b) $Mg_{248}H_{248}$, (c) $Mg_{458}H_{458}$, and (d) $Mg_{1098}H_{1098}$ at 300 K. The (e) external and (f) cutaway views of $Mg_{1098}H_{1098}$ cluster are shown, with the atoms colored with respect to their types of local atomic structures. Green balls represent Mg atoms with crystal structure characteristics, orange balls represents the atoms identified as being on the surface, and other atoms are represented by blue balls.

where N is the number of hydrogen atoms in the cluster, r_i runs over all the positions of those hydrogen atoms. For each time interval t , M nonoverlapping displacements from the position at t_j to $t_j + t$ are calculated. In this work, $t = 1.0$ fs and $M = 50000$ were adopted. For diffusion in three dimensions,

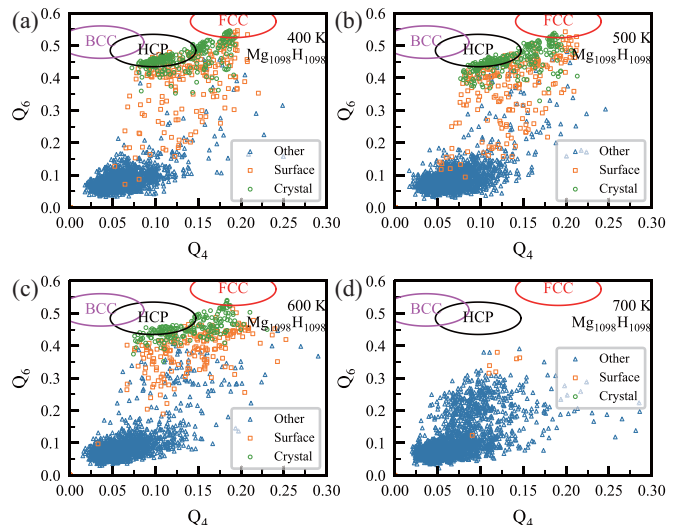


FIG. 11. Correlation maps of BOO parameters Q_4 - Q_6 for $Mg_{1098}H_{1098}$ at (a) 400, (b) 500, (c) 600, and (d) 700 K.

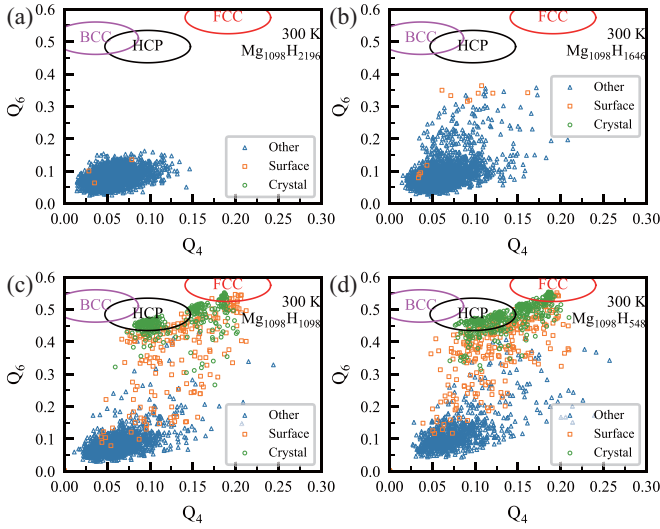


FIG. 12. Correlation maps of BOO parameters Q_4 - Q_6 for (a) $\text{Mg}_{1098}\text{H}_{2196}$, (b) $\text{Mg}_{1098}\text{H}_{1646}$, (c) $\text{Mg}_{1098}\text{H}_{1098}$, and (d) $\text{Mg}_{1098}\text{H}_{548}$ at 300 K.

the diffusion coefficient D can be calculated according to the Einstein equation

$$D = \frac{1}{6} \lim_{t \rightarrow \infty} \frac{d \text{MSD}(t)}{dt}. \quad (12)$$

Figure 13(a) demonstrates that the MSD of hydrogen atoms increases linearly with time, which satisfies the condition of applying Eq. (12) to calculate the diffusion coefficient. For $\text{Mg}_{1098}\text{H}_{2196}$ at 600 K, the calculated diffusion coefficient is $2.47 \times 10^{-9} \text{ m}^2/\text{s}$, which is comparable with the experimental value of $1.25 \times 10^{-9} \text{ m}^2/\text{s}$ at the same temperature reported by Renner and Grabke [114].

The temperature dependence of diffusion coefficient can be interpreted by Arrhenius equation

$$D = D_0 \exp\left(\frac{-E_a}{k_B T}\right), \quad (13)$$

where E_a is the activation energy for hydrogen diffusion, k_B is the Boltzmann constant. The equation indicates a linear relationship between $\ln(D)$ and $1/k_B T$. The Arrhenius plots for $\text{Mg}_{1098}\text{H}_m$ ($m = 548, 1098, 1646, 2196$) are shown in Fig. 13(b), with the temperature ranging from 400 to 700 K. As illustrated, the temperature dependence of the diffusion

coefficient is pronounced in this range that D scales directly with increasing temperature. For each cluster considered, the values of $\ln(D)$ and $1/k_B T$ retain a perfect linear relationship, with a correlation coefficient R^2 greater than 0.997. By fitting the results to the Arrhenius equation, the activation energies of hydrogen diffusion in $\text{Mg}_{1098}\text{H}_{548}$, $\text{Mg}_{1098}\text{H}_{1098}$, $\text{Mg}_{1098}\text{H}_{1646}$, and $\text{Mg}_{1098}\text{H}_{2196}$ are 0.254, 0.248, 0.248 and 0.219 eV, respectively. The difference in activation energy among clusters with different hydrogen contents is small, which explains the experimental observation that D is independent of the applied hydrogen pressure [115].

It is worth noting that at low temperatures, such as 300 K, the results deviate from the linear function obtained by fitting the Arrhenius equation. The number of hydrogen atoms migrating between different positions is low at low temperatures, rendering the MSD mainly coming from the local vibration of hydrogen atoms. This explains the Arrhenius equation only holds within a certain temperature range.

The size of the cluster also affects the diffusion coefficient of H atoms. As shown in Fig. 13(c), at 500 K, D increases as the cluster size decreases. In general, the clusters we calculated conform to this rule, however, with several exceptions. For example, at 500 K, the diffusion coefficient in $\text{Mg}_{458}\text{H}_{686}$ is $D = 1.63 \times 10^{-9} \text{ m}^2/\text{s}$, which is greater than $D = 1.23 \times 10^{-9} \text{ m}^2/\text{s}$ in $\text{Mg}_{248}\text{H}_{372}$. First, for clusters at high temperatures, the energy barriers for hydrogen diffusion decrease dramatically, reducing the differences in activation energies among clusters of different sizes. This makes the values of D to be almost the same in clusters of different sizes, hence the comparison becomes meaningless. Second, the diffusion of hydrogen atoms in clusters exhibited complicated process. Hydrogen atoms can diffuse on the surface, between the surface and the inner layer, among different inner layers, and so forth. The size effect is not limited to the influence of the diameter of the cluster. Other factors, such as specific surface area and surface structure, which originate from different diameters, also affect the diffusion process. Therefore more detailed study is required to get a deeper understanding of the size effect.

V. CONCLUSIONS AND OUTLOOK

In the present work, we developed a machine-learning interatomic potential based on the artificial neural network architecture for Mg-H system. Modified Behler-Parrinello

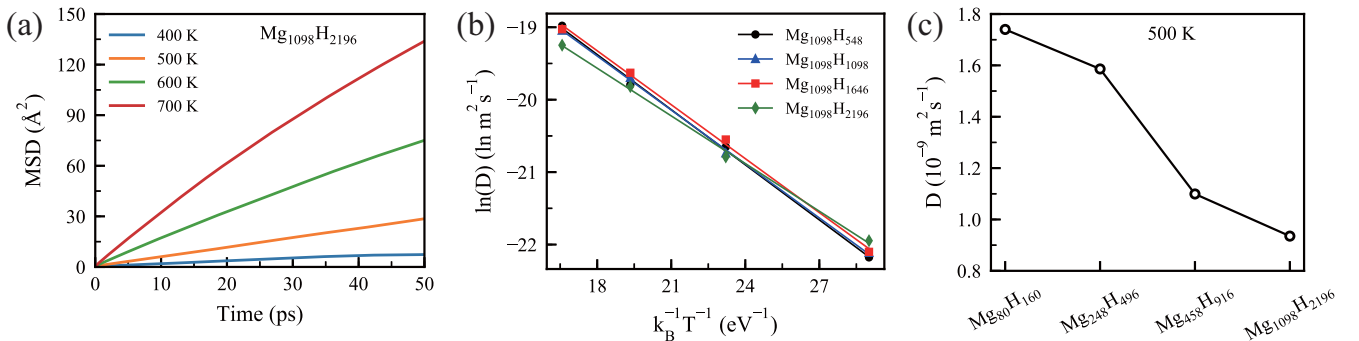


FIG. 13. (a) Mean-squared displacement as a function of time for $\text{Mg}_{1098}\text{H}_{2196}$ at temperatures from 400 to 700 K. (b) The Arrhenius plots for $\text{Mg}_{1098}\text{H}_m$ ($m = 548, 1098, 1646, 2196$). (c) Diffusion coefficients for different sizes of Mg_nH_{2n} ($n = 80, 248, 458, 1098$) clusters at 500 K.

symmetry functions were adopted to describe the local atomic environments. In order to train a relatively general ANN potential suitable for as many conditions as possible, we combined multiple sampling procedures to increase the diversity of the reference samples, including coalescence kick method, *ab initio* MD simulations, and an adaptive sampling strategy. The energies and forces computed by the developed ANN potential can accurately match the DFT calculations of crystal, surface, and cluster structure at any Mg : H ratio. The correct results of bulk properties and phonon dispersions confirm the ability of our ANN potential for calculating crystal structures. The reasonable simulation of H₂ molecules shows the feasibility of our potential to deal with the low-coordinated gas-phase structure. Moreover, the capture of H₂ dissociative adsorption properties on Mg surface proves that our potential is suitable for computing surface structures, and has the prospect of simulating heterogeneous catalytic reactions.

Using the well-trained machine-learning potential, the MD simulations show that phase separation occurs for Mg_nH_m clusters with $m < 2n$. The atomic ratio of Mg : H in the hydride phase is nearly 1 : 2, and the structural properties of the hydride phase is similar to the stoichiometric Mg_nH_{2n} clusters. Ordered geometries are detected in the Mg phase for clusters with a diameter of about 4 nm at temperatures below 600 K. The MD simulation results reveal that the structural properties of the Mg phase are strongly dependent on temperature and cluster size. The spontaneous phase separation of magnesium hydride clusters being observed by theoretical simulations, confirms the rationality of the dehydrogenation

mechanism obtained from the experimental results. Through the calculation of diffusion coefficient, we analyzed the diffusion behavior of hydrogen in the cluster using the MD trajectories. The computed values of D is in good agreement with experimental results, an Arrhenius type temperature dependence is observed in the range of 400 to 700 K. The hydrogen diffusion is independent of the hydrogen contents. As for the effect of cluster size, more detailed calculations are needed, and in general hydrogen atoms diffuse faster in smaller clusters.

Frankly speaking, at about 700 K, the magnesium hydride clusters should start decomposing. However, in our simulations, H₂ releasing was not observed. On one hand, because of the slow kinetics of the MgH₂, the simulation time we run may not long enough for the decomposing process to happen. Note that the ANN potential is still 2 to 3 orders of magnitude slower than the empirical interatomic potentials, which limits our simulation time. On the other hand, although our potential successfully reproduces the H₂ dissociation PES on Mg(0001) surface, the surface complexity of the nanoclusters is much higher, which requires more information about bonding and bond breaking under different surface conditions. Efforts to improve our ANN potential are ongoing in our group, and will be discussed in the future.

ACKNOWLEDGMENT

This work is supported by the National Natural Science Foundation of China (Grant No. 21776004).

-
- [1] L. Schlapbach and A. Züttel, *Nature (London)* **414**, 353 (2001).
 - [2] J. H. Wee, *Renew. Sust. Energ. Rev.* **11**, 1720 (2007).
 - [3] S. Niaz, T. Manzoor, and A. H. Pandith, *Renew. Sust. Energ. Rev.* **50**, 457 (2015).
 - [4] M. Hirscher, V. A. Yartys, M. Baricco, J. B. von Colbe, D. Blanchard, R. C. Bowman, D. P. Broom, C. E. Buckley, F. Chang, P. Chen, Y. W. Cho, J. C. Crivello, F. Cuevas, W. I. F. David, P. E. de Jongh, R. V. Denys, M. Dornheim, M. Felderhoff, Y. Filinchuk, G. E. Froudakis, D. M. Grant, E. M. Gray, B. C. Hauback, T. He, T. D. Humphries, T. R. Jensen, S. Kim, Y. Kojima, M. Latroche, H. W. Li, M. V. Lototsky, J. W. Makepeace, K. T. Müller, L. Naheed, P. Ngene, D. Noréus, M. M. Nygård, S. I. Orimo, M. Paskevicius, L. Pasquini, D. B. Ravnsbæk, M. V. Sofianos, T. J. Udovic, T. Vegge, G. S. Walker, C. J. Webb, C. Weidenthaler, and C. Zlotea, *J. Alloys Compd.* **827**, 153548 (2020).
 - [5] A. Ahmed, S. Seth, J. Purewal, A. G. Wong-Foy, M. Veenstra, A. J. Matzger, and D. J. Siegel, *Nat. Commun.* **10**, 1568 (2019).
 - [6] B. Sakintuna, F. Lamari-Darkrim, and M. Hirscher, *Int. J. Hydrogen Energy* **32**, 1121 (2007).
 - [7] J. C. Crivello, B. Dam, R. V. Denys, M. Dornheim, D. M. Grant, J. Huot, T. R. Jensen, P. de Jongh, M. Latroche, C. Milanese, D. Milčius, G. S. Walker, C. J. Webb, C. Zlotea, and V. A. Yartys, *Appl. Phys. A* **122**, 97 (2016).
 - [8] T. Sadhasivam, H. T. Kim, S. Jung, S. H. Roh, J. H. Park, and H. Y. Jung, *Renew. Sust. Energ. Rev.* **72**, 523 (2017).
 - [9] I. P. Jain, C. Lal, and A. Jain, *Int. J. Hydrogen Energy* **35**, 5133 (2010).
 - [10] E. S. Cho, A. M. Ruminski, Y. S. Liu, P. T. Shea, S. Y. Kang, E. W. Zaia, J. Y. Park, Y. D. Chuang, J. M. Yuk, X. W. Zhou, T. W. Heo, J. H. Guo, B. C. Wood, and J. J. Urban, *Adv. Funct. Mater.* **27**, 1704316 (2017).
 - [11] L. Qian, L. Qin, L. J. Jiang, K. C. Chou, Z. Feng, Z. Qiang, and X. Y. Wei, *J. Alloys Compd.* **359**, 128 (2003).
 - [12] M. Zhu, H. Wang, L. Z. Ouyang, and M. Q. Zeng, *Int. J. Hydrogen Energy* **31**, 251 (2006).
 - [13] A. Schneemann, J. L. White, S. Kang, S. Jeong, L. W. F. Wan, E. S. Cho, T. W. Heo, D. Prendergast, J. J. Urban, B. C. Wood, M. D. Allendorf, and V. Stavila, *Chem. Rev.* **118**, 10775 (2018).
 - [14] D. Tanguy and T. Magnin, *Philos. Mag.* **83**, 3995 (2003).
 - [15] S. Cheung, W. Q. Deng, A. C. T. van Duin, and W. A. Goddard, *J. Phys. Chem. A* **109**, 851 (2005).
 - [16] D. E. Smirnova, S. V. Starikov, and A. M. Vlasova, *Comput. Mater. Sci.* **154**, 295 (2018).
 - [17] X. W. Zhou, S. Kang, T. W. Heo, B. C. Wood, V. Stavila, and M. D. Allendorf, *ChemPhysChem* **20**, 1404 (2019).
 - [18] T. B. Blank, S. D. Brown, A. W. Calhoun, and D. J. Doren, *J. Chem. Phys.* **103**, 4129 (1995).
 - [19] J. Behler and M. Parrinello, *Phys. Rev. Lett.* **98**, 146401 (2007).
 - [20] J. Behler, *Int. J. Quantum Chem.* **115**, 1032 (2015).
 - [21] J. Behler, *Angew. Chem. Int. Ed.* **56**, 12828 (2017).

- [22] A. P. Bartók, M. C. Payne, R. Kondor, and G. Csányi, *Phys. Rev. Lett.* **104**, 136403 (2010).
- [23] A. P. Bartók, R. Kondor, and G. Csányi, *Phys. Rev. B* **87**, 184115 (2013).
- [24] A. P. Bartók and G. Csányi, *Int. J. Quantum Chem.* **115**, 1051 (2015).
- [25] N. Artrith and J. Behler, *Phys. Rev. B* **85**, 045439 (2012).
- [26] S. Chiriki and S. S. Bulusu, *Chem. Phys. Lett.* **652**, 130 (2016).
- [27] S. Chiriki, S. Jindal, and S. S. Bulusu, *J. Chem. Phys.* **146**, 084314 (2017).
- [28] J. Byggmästar, A. Hamedani, K. Nordlund, and F. Djurabekova, *Phys. Rev. B* **100**, 144105 (2019).
- [29] G. C. Sosso, G. Miceli, S. Caravati, J. Behler, and M. Bernasconi, *Phys. Rev. B* **85**, 174103 (2012).
- [30] S. Chiriki, S. Jindal, and S. S. Bulusu, *J. Chem. Phys.* **147**, 154303 (2017).
- [31] S. Hajinazar, J. P. Shao, and A. N. Kolmogorov, *Phys. Rev. B* **95**, 014114 (2017).
- [32] N. Artrith, T. Morawietz, and J. Behler, *Phys. Rev. B* **83**, 153101 (2011).
- [33] N. Artrith and A. Urban, *Comput. Mater. Sci.* **114**, 135 (2016).
- [34] K. V. J. Jose, N. Artrith, and J. Behler, *J. Chem. Phys.* **136**, 194111 (2012).
- [35] M. Gastegger and P. Marquetand, *J. Chem. Theory Comput.* **11**, 2187 (2015).
- [36] M. Gastegger, C. Kauffmann, J. Behler, and P. Marquetand, *J. Chem. Phys.* **144**, 194110 (2016).
- [37] J. Behler, R. Martoňák, D. Donadio, and M. Parrinello, *Phys. Rev. Lett.* **100**, 185501 (2008).
- [38] J. R. Boes, M. C. Groenenboom, J. A. Keith, and J. R. Kitchin, *Int. J. Quantum Chem.* **116**, 979 (2016).
- [39] J. R. Boes and J. R. Kitchin, *Mol. Simul.* **43**, 346 (2017).
- [40] J. Behler, *Phys. Chem. Chem. Phys.* **13**, 17930 (2011).
- [41] J. S. Smith, O. Isayev, and A. E. Roitberg, *Chem. Sci.* **8**, 3192 (2017).
- [42] J. Behler, *J. Chem. Phys.* **134**, 074106 (2011).
- [43] N. Artrith, B. Hiller, and J. Behler, *Phys. Status Solidi B* **250**, 1191 (2013).
- [44] K. Hornik, *Neural Netw.* **4**, 251 (1991).
- [45] K. Miwa and H. Ohno, *Phys. Rev. B* **94**, 184109 (2016).
- [46] B. Onat, E. D. Cubuk, B. D. Malone, and E. Kaxiras, *Phys. Rev. B* **97**, 094106 (2018).
- [47] P. Rowe, G. Csányi, D. Alfè, and A. Michaelides, *Phys. Rev. B* **97**, 054303 (2018).
- [48] J. E. Herr, K. Yao, R. McIntyre, D. W. Toth, and J. Parkhill, *J. Chem. Phys.* **148**, 241710 (2018).
- [49] N. Artrith, A. Urban, and G. Ceder, *J. Chem. Phys.* **148**, 241711 (2018).
- [50] S. D. Huang, C. Shang, X. J. Zhang, and Z. P. Liu, *Chem. Sci.* **8**, 6327 (2017).
- [51] S. D. Huang, C. Shang, P. L. Kang, and Z. P. Liu, *Chem. Sci.* **9**, 8644 (2018).
- [52] S. C. Ma, C. Shang, and Z. P. Liu, *J. Chem. Phys.* **151**, 050901 (2019).
- [53] W. Ibarra-Hernández, S. Hajinazar, G. Avendaño-Franco, A. Bautista-Hernández, A. N. Kolmogorov, and A. H. Romero, *Phys. Chem. Chem. Phys.* **20**, 27545 (2018).
- [54] B. B. Averkiev, Ph.D. thesis, Utah State University, 2009.
- [55] H. C. Zhai, M. A. Ha, and A. N. Alexandrova, *J. Chem. Theory Comput.* **11**, 2385 (2015).
- [56] D. Shen, C. P. Kong, R. Jia, P. Fu, and H. X. Zhang, *J. Phys. Chem. A* **119**, 3636 (2015).
- [57] T. R. Galeev, A. S. Ivanov, C. Romanescu, W. L. Li, K. V. Bozhenko, L. S. Wang, and A. I. Boldyrev, *Phys. Chem. Chem. Phys.* **13**, 8805 (2011).
- [58] M. Gastegger, J. Behler, and P. Marquetand, *Chem. Sci.* **8**, 6924 (2017).
- [59] N. Bernstein, G. Csányi, and V. L. Deringer, *NPJ Computat. Mater.* **5**, 99 (2019).
- [60] S. De, A. P. Bartók, G. Csányi, and M. Ceriotti, *Phys. Chem. Chem. Phys.* **18**, 13754 (2016).
- [61] J. Mavračić, F. C. Mocanu, V. L. Deringer, G. Csányi, and S. R. Elliott, *J. Phys. Chem. Lett.* **9**, 2985 (2018).
- [62] M. A. Caro, A. Aarva, V. L. Deringer, G. Csányi, and T. Laurila, *Chem. Mater.* **30**, 7446 (2018).
- [63] A. R. Oganov and M. Valle, *J. Chem. Phys.* **130**, 104504 (2009).
- [64] V. L. Deringer and G. Csányi, *Phys. Rev. B* **95**, 094203 (2017).
- [65] H. S. Seung, M. Opper, and H. Sompolinsky, in *Proceedings of The Fifth Annual Workshop on Computational Learning Theory*, COLT (Association for Computing Machinery, New York, USA, 1992), pp. 287–294.
- [66] J. S. Smith, B. Nebgen, N. Lubbers, O. Isayev, and A. E. Roitberg, *J. Chem. Phys.* **148**, 241733 (2018).
- [67] A. P. Bartók, J. Kermode, N. Bernstein, and G. Csányi, *Phys. Rev. X* **8**, 041048 (2018).
- [68] D. Dragoni, T. D. Daff, G. Csányi, and N. Marzari, *Phys. Rev. Mater.* **2**, 013808 (2018).
- [69] A. Pukrittayakamee, M. Malshe, M. Hagan, L. M. Raff, R. Narulkar, S. Bukkapatnam, and R. Komanduri, *J. Chem. Phys.* **130**, 134101 (2009).
- [70] H. T. Nguyen-Truong and H. M. Le, *Chem. Phys. Lett.* **629**, 40 (2015).
- [71] R. H. Ouyang, Y. Xie, and D. E. Jiang, *Nanoscale* **7**, 14817 (2015).
- [72] S. Jindal, S. Chiriki, and S. S. Bulusu, *J. Chem. Phys.* **146**, 204301 (2017).
- [73] N. Artrith and A. M. Kolpak, *Comput. Mater. Sci.* **110**, 20 (2015).
- [74] N. Artrith and A. M. Kolpak, *Nano Lett.* **14**, 2670 (2014).
- [75] J. Kang, S. H. Noh, J. Hwang, H. Chun, H. Kim, and B. Han, *Phys. Chem. Chem. Phys.* **20**, 24539 (2018).
- [76] S. Hajinazar, E. D. Sandoval, A. J. Cullo, and A. N. Kolmogorov, *Phys. Chem. Chem. Phys.* **21**, 8729 (2019).
- [77] M. Y. Song, J.-P. Manaud, and B. Darriet, *J. Alloys Compd.* **282**, 243 (1999).
- [78] M. Y. Song, *Int. J. Hydrogen Energy* **28**, 403 (2003).
- [79] G. Kresse and J. Furthmüller, *Phys. Rev. B* **54**, 11169 (1996).
- [80] G. Kresse and D. Joubert, *Phys. Rev. B* **59**, 1758 (1999).
- [81] J. P. Perdew, K. Burke, and M. Ernzerhof, *Phys. Rev. Lett.* **77**, 3865 (1996).
- [82] T. Morawietz and J. Behler, *J. Phys. Chem. A* **117**, 7356 (2013).
- [83] S. Grimme, J. Antony, S. Ehrlich, and H. Krieg, *J. Chem. Phys.* **132**, 154104 (2010).
- [84] S. Grimme, S. Ehrlich, and L. Goerigk, *J. Comput. Chem.* **32**, 1456 (2011).
- [85] K. Yao, J. E. Herr, D. W. Toth, R. Mckintyre, and J. Parkhill, *Chem. Sci.* **9**, 2261 (2018).

- [86] S. R. Bahn and K. W. Jacobsen, *Comput. Sci. Eng.* **4**, 56 (2002).
- [87] A. H. Larsen, J. J. Mortensen, J. Blomqvist, I. E. Castelli, R. Christensen, M. Dulak, J. Friis, M. N. Groves, B. Hammer, C. Hargus, E. D. Hermes, P. C. Jennings, P. B. Jensen, J. Kermode, J. R. Kitchin, E. L. Kolsbjerg, J. Kubal, K. Kaasbjerg, S. Lysgaard, J. B. Maronsson, T. Maxson, T. Olsen, L. Pastewka, A. Peterson, C. Rostgaard, J. Schiützt, O. Schütt, M. Strange, K. S. Thygesen, T. Vegge, L. Vilhelmsen, M. Walter, Z. H. Zeng, and K. W. Jacobsen, *J. Phys.: Condens. Matter* **29**, 273002 (2017).
- [88] A. Togo and I. Tanaka, *Scripta Mater.* **108**, 1 (2015).
- [89] L. Chaput, A. Togo, I. Tanaka, and G. Hug, *Phys. Rev. B* **84**, 094302 (2011).
- [90] P. Vajeeston, P. Ravindran, A. Kjekshus, and H. Fjellvåg, *Phys. Rev. Lett.* **89**, 175506 (2002).
- [91] T. Kelkar and S. Pal, *J. Mater. Chem.* **19**, 4348 (2009).
- [92] P. Vajeeston, P. Ravindran, B. C. Hauback, H. Fjellvåg, A. Kjekshus, S. Furuseth, and M. Hanfland, *Phys. Rev. B* **73**, 224102 (2006).
- [93] M. de Jong, W. Chen, T. Angsten, A. Jain, R. Notestine, A. Gamst, M. Sluiter, C. K. Ande, S. van der Zwaag, J. J. Plata, C. Toher, S. Curtarolo, G. Ceder, K. A. Persson, and M. Asta, *Sci. Data* **2**, 150009 (2015).
- [94] S. Cui, W. Feng, H. Hu, Z. Feng, and Y. Wang, *Solid State Commun.* **148**, 403 (2008).
- [95] F. D. Murnaghan, *Proc. Natl. Acad. Sci. USA* **30**, 244 (1944).
- [96] F. Birch, *Phys. Rev.* **71**, 809 (1947).
- [97] M. Hebbache and M. Zemzemi, *Phys. Rev. B* **70**, 224107 (2004).
- [98] J. Lasave, F. Dominguez, S. Koval, M. G. Stachiotti, and R. L. Migoni, *J. Phys.: Condens. Matter* **17**, 7133 (2005).
- [99] S. Mehta, G. D. Price, and D. Alfè, *J. Chem. Phys.* **125**, 194507 (2006).
- [100] X. W. Zhou, D. K. Ward, M. Foster, and J. A. Zimmerman, *J. Mater. Sci.* **50**, 2859 (2015).
- [101] T. Vegge, *Phys. Rev. B* **70**, 035412 (2004).
- [102] B. Hammer, L. B. Hansen, and J. K. Nørskov, *Phys. Rev. B* **59**, 7413 (1999).
- [103] A. J. Du, S. C. Smith, X. D. Yao, and G. Q. Lu, *J. Phys. Chem. B* **109**, 18037 (2005).
- [104] T. Schneider and E. Stoll, *Phys. Rev. B* **17**, 1302 (1978).
- [105] X. L. Ma, S. G. Liu, and S. P. Huang, *Int. J. Hydrogen Energy* **42**, 24797 (2017).
- [106] P. J. Steinhardt, D. R. Nelson, and M. Ronchetti, *Phys. Rev. B* **28**, 784 (1983).
- [107] W. Lechner and C. Dellago, *J. Chem. Phys.* **129**, 114707 (2008).
- [108] M. Leocmach, PYBOO: A PYTHON package to compute bond orientational order parameters (2017), <https://github.com/MathieuLeocmach/pyboo>.
- [109] M. Leocmach and H. Tanaka, *Nat. Commun.* **3**, 974 (2012).
- [110] T. R. Jensen, A. Andreasen, T. Vegge, J. W. Andreasen, K. Ståhl, A. S. Pedersen, M. M. Nielsen, A. M. Molenbroek, and F. Besenbacher, *Int. J. Hydrogen Energy* **31**, 2052 (2006).
- [111] A. S. Gangrade, A. A. Varma, N. K. Gor, S. Shrinivasan, and S. S. V. Tatiparti, *Phys. Chem. Chem. Phys.* **19**, 6677 (2017).
- [112] A. Zaluska, L. Zaluski, and J. O. Ström-Olsen, *J. Alloys Compd.* **288**, 217 (1999).
- [113] B. Vegholm, K. Jensen, B. Larsen, and A. S. Pedersen, *J. Less-Common Metals* **131**, 133 (1987).
- [114] J. Renner and H. J. Grabke, *Z. Metallkd.* **69**, 639 (1978).
- [115] C. Nishimura, M. Komaki, and M. Amano, *J. Alloys Compd.* **293-295**, 329 (1999).